Journal of Hydraulic Research

ISSN: (Print) (Online) Journal homepage: www.tandfonline.com/journals/tjhr20

Spatiotemporal evolution of mine tailings released in sand-bed rivers

Andrés F. Rojas-Aguirre & Marcelo H. Garcia

To cite this article: Andrés F. Rojas-Aguirre & Marcelo H. Garcia (2025) Spatiotemporal evolution of mine tailings released in sand-bed rivers, Journal of Hydraulic Research, 63:1, 64-87, DOI: 10.1080/00221686.2024.2446567

To link to this article: https://doi.org/10.1080/00221686.2024.2446567

Published online: 10 Feb 2025.

JOURNAL OF HYDRAULIC RESEARCH
2025, VOL. 63, NO. 1, 64–87
https://doi.org/10.1080/00221686.2024.2446567

International Association for Hydro-Environment Engineering and Research

Taylor & Francis
Taylor & Francis Group

RESEARCH PAPER

Spatiotemporal evolution of mine tailings released in sand-bed rivers

Andrés F. Rojas-Aguirre and Marcelo H. Garcia

Ven Te Chow Hydrosystems Laboratory, Department of Civil and Environmental Engineering, The Grainger College of Engineering, University of Illinois Urbana-Champaign, Urbana, IL, USA

ABSTRACT

The dispersion and fate of mine tailings in riverine systems are studied through classical morphodynamic evolution analysis. This paper develops a 1D sediment formulation to assess the long-term spatiotemporal evolution and spreading of a single iron-ore tailings pulse deposited in the Paraopeba River (Brazil) in 2019. In this numerical analysis, sediment density is used as a surrogate to track the tailings along the river within the active layer and substrate. Based on observed data, the Sorting Engelund-Hansen Equation (SEH) for sand-bed rivers was recalibrated, since its parameters were based on large flume experiments and were limited to ambient sediment material. The simulation results align with observed tailings spreading, showing bed aggradation in low-velocity zones, such as the pool upstream of the Igarapé spillway, a suitable location for monitoring and control.The rapid bed degradation near the source zone (Ferro Carvão Creek confluence) is explained, as this material easily entrains into suspension.

ARTICLE HISTORY
Received 15 May 2024
Accepted 13 December 2024
Open for discussion

KEYWORDS
Bedrock outcrops; Engelund–Hansen equation; Exner equation; iron tailings; Paraopeba River; sediment density

1. Introduction

The continuous release of mine tailings into river systems has severely impacted river networks, causing widespread environmental damage that extends for hundreds of kilometres (Hudson-Edwards, 2016). For instance, the Ok Tedi copper mine located in Papua New Guinea is a well-known case where mine tailings and rock material have been continuously released into its headwaters since 1984 (Cui & Parker, 1999). Another notable case is the persistent and long-term discharge of arsenic tailings into the Fourche River (South Dakota, USA), spanning over a century (Marron, 1989).

Instantaneous releases of mine tailings have gained worldwide attention due to the accidental spills into water bodies, especially after three recent dam breach incidents that occurred in the past decade. The first incident occurred in 2014 at Mount Polley mine, where approximately 25 Mm^3 of mine waste was released into Quesnel Lake (Granger et al., 2022). The second incident took place on 5 November 2015, at the Fundão tailings dam in Mariana (Minas Gerais, Brazil), releasing around 43 Mm^3 of iron mine tailings (do Carmo et al., 2017). This incident destroyed the town of Benito Rodrigues and caused environmental impacts that extended over 670 km along the Doce River (Palu & Julien, 2019). The third incident happened on 25 January 2019, near Brumadinho (Minas Gerais, Brazil) and caused environmental damage along the Ferro Carvão Creek and Paraopeba River. According to Robertson et al. (2019), around 9.7 Mm^3 of tailings were released from the Córrego do Feijão Iron Ore Mine (Barragem B-1 or Dam B-I). These tailings travelled downhill and reached the Paraopeba River, 10 km away from Dam B-I, with an estimated volume of 1.6 Mm^3 (Laureano et al., 2022).

These significant dam breach accidents have motivated different researchers to implement and improve numerical models as a tool to assess the potential risk of tailings dam breaches worldwide. Commercial and non-commercial models (FLOW-3D, FLO-2D, DAN3D, HEC-RAS, EMBREA-MUD, Riverflow2D) have been implemented, developed, validated and adapted to simulate these dam breach accidents (Ghahramani et al., 2022; Gibson et al., 2022; Lumbroso et al., 2021; Martínez-Aranda et al., 2022; Wang et al., 2020). However, less attention has been focused on the transport characteristics of tailings materials that reach and move along watercourses.

Some previous efforts include the implementation of one-dimensional (1D) numerical models to predict the long- and short-term spreading of tailings in riverine systems. These models can be divided into two: washload models and bed sediment models. The former treat the tailings as a dissolved contaminant, applying the advection-dispersion equation (ADE) with sink or source terms that represent the transformation processes affecting the tailings (Lindenschmidt et al., 2022; Palu & Julien, 2019). The second type of model is mainly based on three elements: (1) a sediment conservation equation (i.e. Exner equation), (2) a formulation

CONTACT Andrés F. Rojas-Aguirre afr3@illinois.edu

describing the interaction between the water column and the riverbed (e.g. active layer theory), and (3) a sediment transport equation to estimate the sediment volume or sediment transport rates.

For the case of the tailings released into the Doce River (due to the dam breach of the Fundão dam), the plume of tailings was tracked by indirectly measuring the suspended sediment concentrations (SSC) along the river (CPRM-ANA, 2015). Palu and Julien (2019) demonstrated that a calibrated one-dimensional advection-dispersion equation (ADE) is a suitable tool to represent the wave of suspended sediments that travelled along the river system right after the accident. This tool allowed these researchers to assess the peak concentrations expected for hypothetical scenarios, such as the absence of water reservoirs along the Doce River.

The second type of models has been implemented to study and predict the spreading of the iron tailings in the Paraopeba River by using the 1-D HEC-RAS model (Vale & Potamos, 2020). As this model does not consider sediment fractions with different densities, Salgado Terêncio et al. (2023) addressed this limitation employing the RiverFLOW2D model to assess the suspended sediment retention at a 6 m-height spillway located in the Paraopeba River at the municipality of Jautuba (Minas Gerais, Brazil). However, this model does not include a stratigraphy module that can be useful to evaluate the evolution of the sediment deposition in low-velocity zones (e.g. upstream of the spillway). Keeping track of the sediments in the bed is crucial.

To overcome previous limitations, herein we propose an approach to distinguish and track material with different densities and fractions along riverine systems. This approach enables us to track the iron tailings by using the density of the sediments as a surrogate to track and determine the location of iron tailings in the Paraopeba River. Although current models (e.g. Telemac, RiverFlow2D) can be used to determine the spatial distribution density of the sediment material in rivers, our approach introduces a mathematical formulation that incorporates the rate of change of sediment density and the mean sediment size in the active layer – factors often overlooked. Also, this mathematical formulation is developed based on the physical phenomena seen in the field measurements taken along the Paraopeba River. This mathematical formulation is based on the active layer concept (Hirano, 1971), the grain-size mass balance proposed by Parker (1991), the exchange fractions proposed by Hoey and Ferguson (1994) and the stratigraphic model developed by Viparelli et al. (2010).

Additionally, the previous numerical efforts were performed assuming that the transport of tailings in fluvial environments is analogous to that of the natural sediments (Berenbrock & Tranmer, 2008; Cui & Parker, 1999). The presence of fine and dense tailings results in modifications of the traditional total bed sediment transport formulations since most of them were derived from natural sediments (e.g. Brownlie, 1981; Engelund & Hansen, 1967; Karim, 1981; Molinas & Wu, 2010; C. T. Yang, 1973). To overcome this limitation, this modelling effort includes the recalibration of the Sorting Engelund-Hansen (SEH) equation (An et al., 2020; Naito et al., 2019) to estimate the sand–tailings transport rates along the Paraopeba River.

In this study, we conduct a long-term numerical simulation to track iron-ore tailings along the Paraopeba River by implementing the proposed mathematical formulation alongside the calibrated SEH transport equation. The simulation employs a representative, constant flow discharge condition (i.e. dominant discharge) and uses sediment density as a surrogate to track the location of the iron-ore tailings within both the active layer and the substrate. This analysis does not intend to provide a detailed representation of the riverbed and sediment density evolution under historical conditions, as these are functions of different factors such as the hydrology of the basin, the water releases from the dammed tributaries, and ongoing dredging operations to remove iron-ore tailings near the Ferro-Carvão confluence in the Paraopeba River.

The structure of this paper is as follows: In Section 2, we describe the numerical model setup and dataset used in this work. In Section 3, we present the results and the analysis for simplified conditions in the Paraopeba River. Finally, the conclusions of this study are summarized in Section 4.

2. Methods

2.1. Site description

The course of the Paraopeba River runs about 510 km in the N–NW direction from its headwaters (close to the municipality of Cristiano Otoni) to its mouth in the Três Marias Reservoir (municipality of Felixlândia) in the state of Minas Gerais. Its drainage basin is approximately 13,000 km^2 with 35 municipalities and a population of about 1.3 million people (IBGE, 2010). The remnants of Dam B-I are located in a subbasin of a tributary of the Paraopeba River, associated with the Ferro Carvão Creek, whose drainage basin covers 32.8 km^2 (CPRM, ANA, COPASA, & IGAM, 2019). The initial mound of iron tailings released in the Paraopeba River extended over 6 km approximately, with its starting point being around half a kilometre upstream of the Ferro Carvão Creek confluence.

The study domain for this work corresponds to a 295 km subreach of the Paraopeba River starting from the Melo Franco municipality (which is located 10 km upstream of the Ferro Carvão Creek confluence) and

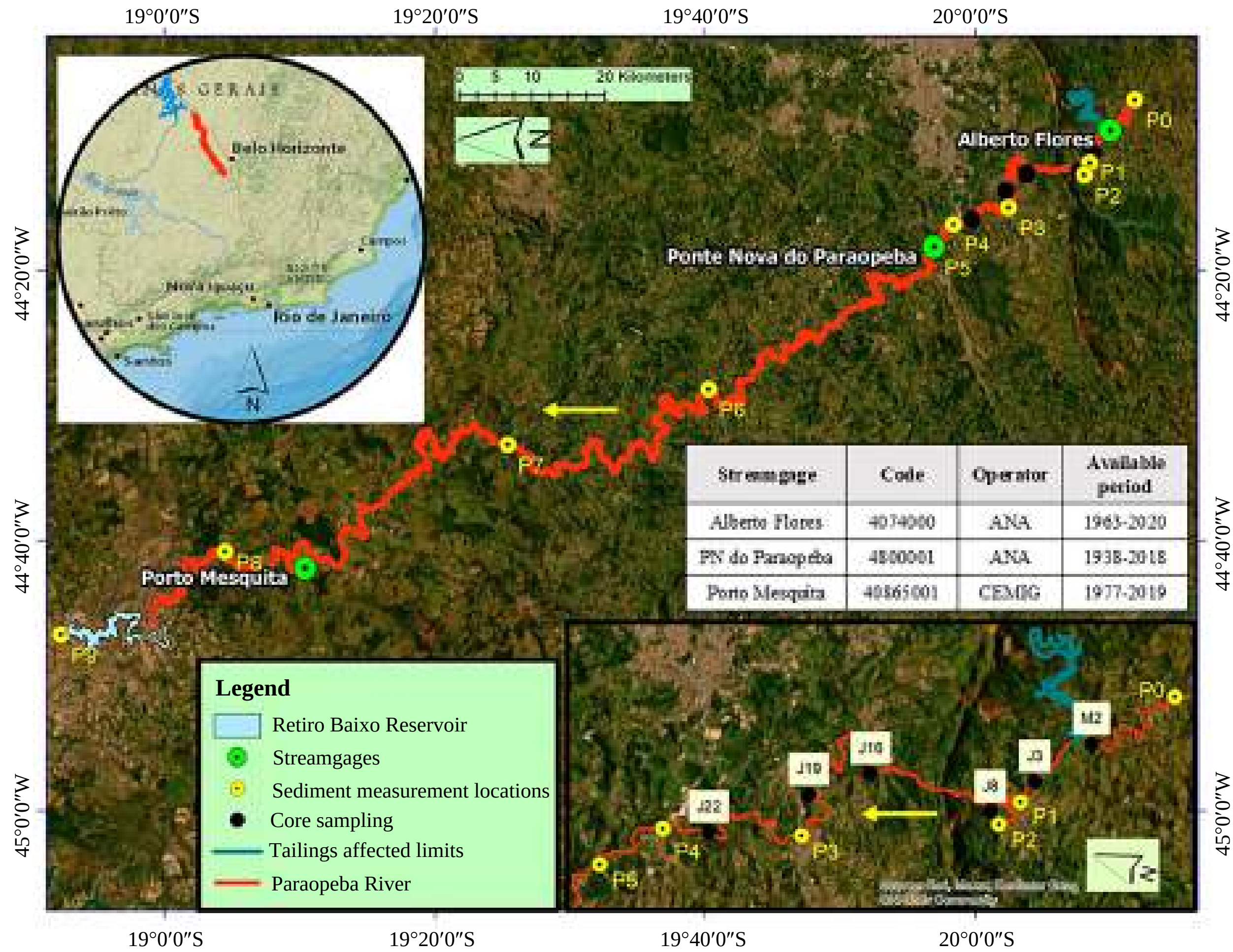

Figure 1. Study domain, streamgages, core sampling and sediment measurement locations.

extending up to the Retiro Baixo Reservoir, situated at the boundary between the Curvelo and Pompéu municipalities (Figure 1). It is essential to highlight the presence of a 6.0 m height spillway that was constructed to withdraw water for the Igarapé Thermal Power Station located in the municipality of Jatuba (47 km downstream of the Ferro Carvão Creek confluence). This structure will hereafter be referred to as the spillway at Igarapé.

The mean longitudinal slopes in this subreach range from 0.04% to 0.07% with some bedrock outcrops and cascades that control the vertical and lateral erosion of the river.

2.2. Datasets

To define the initial and boundary conditions for our numerical model, we used the sediment and flow discharge datasets prior to and after the arrival of the iron tailings into the Paraopeba River. The river conditions prior to the arrival of the iron tailings were assessed using the historical records from streamgages operated by the Natural Water Agency of Brazil (Agência Nacional de Águas, ANA) and the Brazilian Power Company of the State of Minas Gerais (Companhia Energética de Minas Gerais, CEMIG). These records contain time-series of stages and discharges, and only two streamgages report suspended sediment measurements (Ponte Nova do Paraopeba, and Porto Mesquita). To assess the conditions after the arrival of the iron tailings, we used another dataset from multiple field campaigns conducted along the river from a subreach of the Paraopeba River that spans from 10 km upstream of the confluence of the Ferro Carvão Creek (close to the Melo Franco municipality) to the downstream end of the Retiro Baixo Reservoir (Figure 1). These campaigns conducted by Vale include flow measurements, collection of sediment samples, and bathymetries at 10 different sites (P0 to P9). These *in situ* measurements were complemented with laboratory analyses to determine the granular size distribution (GSD), the suspended sediment concentrations (SSC), and the density of the bed material.

To characterize the substrate from the first 6 km downstream of the Ferro Carvão Creek confluence, we used a 3D representation model of the substrate based on the information from multiple core samples and acoustic Doppler current profiler (ADCP) bathymetries conducted in 2019, 2020 and 2021 (Vale & Saga, 2021). Additionally, we considered in this study a dataset from 26 core samples collected at sediment bars and banks from Melo Franco to right downstream

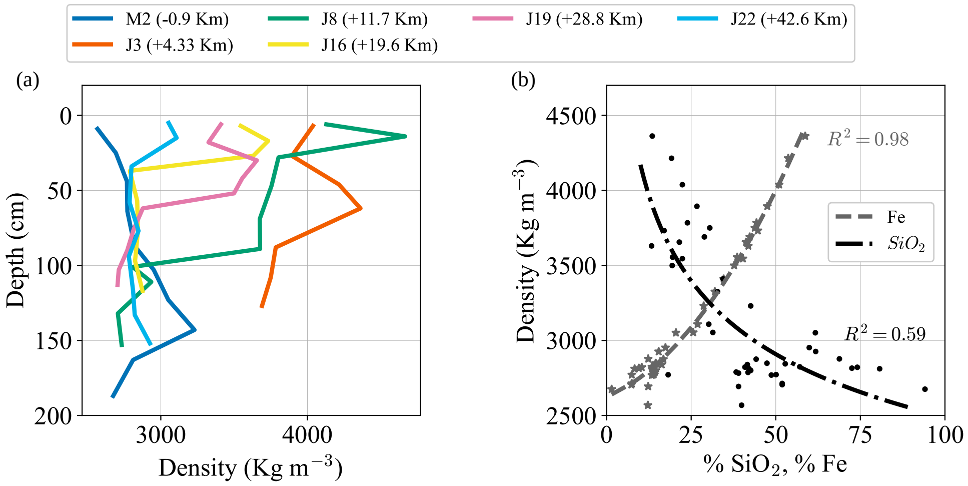

Figure 2. (a) Vertical profiles of density at six distinct locations along the reach from Melo Franco to downstream of the Igarapé spillway (the location of this core samples is depicted in Figure 1; the negative sign corresponds to the distance upstream from Ferro Carvão confluence, while positive values refer to downstream distances). (b) Correlation between density of core samples and the amount of iron (Fe) and silicon dioxide (SiO_2).

the spillway at Igarapé (Laureano et al., 2022; Vale & Arcardis, 2020).

Likewise, for this study we used bathymetric survey information conducted by Vale S.A. in February 2019, October 2020 and September 2021. These surveys combined ADCP data with cross-sectional measurements. The 2019 survey was used in this work for the subreach downstream of the spillway at Igarapé and the subreach upstream of the Carvão confluence, while the 2020 survey was used for the subreach between the Ferro Carvão confluence and the spillway.

2.3. Tracking iron tailings

Based on the physicochemical characterization of 54 samples at six different locations from the core sampling dataset conducted at the sediment bars and banks (Figure 2a), we found high correlation between the content of iron and the density of the material ($R^2 = 0.98$) and a moderate correlation between the density and silicon dioxide, SiO_2 (Figure 2b). The reason for these correlations is due to the high content of ferruginous species where hematite, magnetite and goethite prevail (92.7%), while the content of quartz is relatively low (Robertson et al., 2019). This finding allows us to use the density of the sand–tailings mixture as a surrogate to track the iron-ore tailings along the river.

The sediment conservation equations proposed herein are based on the active layer concept, originally proposed by Hirano (1971). This approach divides the bed into two main regions: an active layer and the substrate layer. The substrate layer is viewed as the volume of material for which all sediment grains have a null probability of entrainment into the water column, conversely to the active layer (immediately beneath the sediment-water flow interface) in which the probability of entrainment is uniform. When deposition (aggradation) occurs, some material from the active layer becomes part of the substrate. Conversely, during erosion, the process is reversed, with substrate material potentially being incorporated back into the active layer. Therefore, sediment in the substrate can indeed re-enter the water column during erosion. However, this can only happen after the substrate material has transitioned into the active layer. Once in the active layer, the sediment particles can be entrained into the water column with a uniform probability.

The one-dimensional (1D) sediment conservation equation derivation is similar to the one reported by Parker (1991, 2004). However, in this case, we considered the density variation in the control volume (Figure 3). Thus, instead of writing these equations in terms of volume rate per unit width, we rather work with mass transport rate per unit width. Also, as the bedrock controls the river vertically, we only considered the layers above the elevation of the bedrock material, η_b (Equation (1a)). The bed material mass conservation equation is given by:

$$\frac{\partial}{\partial t}\int_{\eta_b}^{\eta} \rho_i' f_i' (1-\lambda_p)\Delta x \, dz = \left[g_{Ti}|_x - g_{Ti}|_{x+\Delta x} \right] \quad (1a)$$

$$(1-\lambda_p)\frac{\partial}{\partial t}\int_{\eta_b}^{\eta} \rho_i' f_i' \, dz = -\frac{\partial}{\partial x} g_{Ti} \quad (1b)$$

where t denotes time; x is the streamwise direction coordinate; z is the upward coordinate; λ_p is the porosity; η is the channel bed elevation; η_b is the elevation of the bedrock; g_{Ti} is the total mass transport rate per unit width for ith fraction ($g_{Ti} = q_{Ti}\rho_i$); and ρ_i' and f_i' are the density and volume fractions, respectively, defined as:

$$\rho_i' f_i'(x,z,t) = \begin{cases} \rho_i F_i(x,z,t), & \eta - L_a < z < \eta \\ \rho_{si} f_i(x,z), & \eta_b < z \le \eta - L_a \end{cases} \quad (2)$$

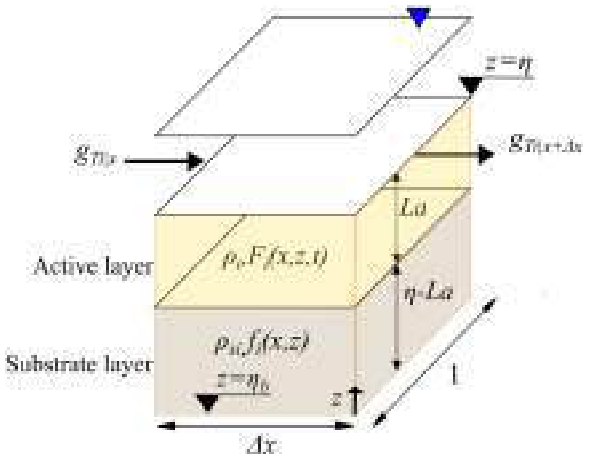

Figure 3. Active layer concept using two layers: active layer, and substrate. The active layer has no sediment structure, and its density for the *i*th fraction ρ_i and its sediment fraction F_i vary over time. Conversely, the density in the substrate ρ_{si} and the corresponding fractions (f_i) have no variation in time. Modified from Hirano (1971).

where F_i and f_i are the fractions in the active layer and the substrate, respectively; L_a is the active layer thickness; and ρ_i and ρ_{si} are the density fractions in the active layer and the substrate, respectively.

Considering the fractions and densities in the *i*th fraction, we derive a 1D mass conservation equation for different fractions and densities (Equation (3)). The derivation of the following equations is included in Appendix 1.

$$(1-\lambda_p)\left[(F_i\rho_i-\rho_{Ii}f_{Ii})\frac{\partial L_a}{\partial t}+\rho_{Ii}f_{Ii}\frac{\partial \eta}{\partial t}+L_a\frac{\partial F_i\rho_i}{\partial t}\right] = -\frac{\partial q_{Ti}}{\partial x} \quad (3)$$

where $\rho_{Ii}f_{Ii}$ is the interfacial density exchange fraction given by Equation (4), based on the original concept proposed by Hoey and Ferguson (1994). This term describes the sediment density exchange between the active and substrate layers as the bed aggrades or degrades (Equation (4)):

$$\rho_{Ii}f_{Ii}=\begin{cases}\rho_{si}f_i, & \dfrac{\partial\eta}{\partial t}<0\\ \alpha F_i\rho_i+(1-\alpha)\times p_i\rho_{i,j}, & \dfrac{\partial\eta}{\partial t}>0\end{cases} \qquad p_i=\frac{g_{Ti}}{g_T} \quad (4)$$

where α is a weight factor that ranges between 0 and 1.

The reason for choosing the Hoey and Ferguson (1994) approach is that during the deposition case (i.e. $\partial\eta/\partial t>0$), the contribution to this exchange density fraction of the fractions of the active layer and the sediment transport fractions can be modified. The density peaks underneath the active layer in the vertical profiles at all locations downstream of the confluence (Figure 2a indicates a substantial contribution of the sediment transport fractions to the substrate layers). Thus, not all suspended sediment fractions mix entirely in the active layer since some fractions are pushed down to the substrate. As a consequence, the $1-\alpha$ term is not negligible.

Summing over all the fractions described in Equation (3), the evolution of the bed elevation is described by Equation (5):

$$\frac{\partial\eta}{\partial t}=-\frac{1}{\rho_I(1-\lambda_p)}\frac{\partial g_T}{\partial x}-\left(\frac{\rho_a}{\rho_I}-1\right)\frac{\partial L_a}{\partial t}-\frac{L_a}{\rho_I}\frac{\partial\rho_a}{\partial t} \quad (5)$$

where $\rho_I=\sum_{n=1}^{N}f_{Ii}\rho_{Ii}$, and $\rho_a=\sum\rho_iF_i$.

2.3.1. Stratigraphy in the substrate

As the iron tailings deposited in the Paraopeba River are subjected to significant aggradation and erosion processes, this formulation effort incorporates a stratigraphy analysis to predict the spatiotemporal distribution of the iron tailings in the substrate. In lieu of considering a homogeneous substrate, we use a stratification approach in which the volume f_i and density ρ_{si} fractions exhibit a vertical variation. The inclusion of the density in the different layers is an extension of the numerical method originally proposed by Viparelli et al. (2010) in which the substrate is discretized in multiple layers of uniform thickness, L_s, except at the topmost layer (underneath the active layer) where the thickness, L_b, varies according to the aggradation and degradation processes that occur at each node or cross-section j (Figure 4).

During aggradation, the magnitudes of $f_{i,j,M}$ and $\rho_{si,i,j,M}$ at the topmost layer (M), are estimated based on a mixture between the materials in the active layer and the topmost layer of the substrate. In the case of $L_b>L_s$, a new layer is created, and $\rho_{si,i,j,M}f_{i,j,M}$ is calculated by estimating the weighted average of the new and previous magnitudes based on Equation (6); otherwise (i.e. $L_b\le L_s$), $\rho_{si,i,j,M}f_{i,j,M}$ is estimated according to Equation (7), as follows:

$$\rho_{si,i,j,M}f_{i,j,M}|_{t+\Delta t}=\frac{\rho_{i,j,M-1}f_{i,j,M-1}[\eta_{int,j}-(M_j-2)L_s]|_t+[(M_j-1)L_s-\eta_{int,j}]|_t f_{Ii,j}\rho_{Ii,j}}{L_s} \quad (6)$$

$$\rho_{si,i,j,M}f_{i,j,M}|_{t+\Delta t}=\frac{\rho_{i,j,M}f_{i,j,M}[\eta_{int,j}-(M_j-2)L_s]|_t+\delta_j\rho_{Ii,j}f_{Ii,j}}{[\eta_{int}-(M_j-2)L_s]|_t+\delta_j} \quad (7)$$

$$\delta_j=\eta_{int,j}|_{t+\Delta t}-\eta_{int,j}|_t$$

where the subscript j indicates the nodes in the substrate at control volume j; the subscript i refers to the *i*th grain size fraction; η_{int} is the elevation of the interface substrate layer; M_j refers to the number of vertical nodes at cross-section j; $\rho_{Ii,j}f_{Ii,j}$ is estimated using Equation (4); and Δt is the time step.

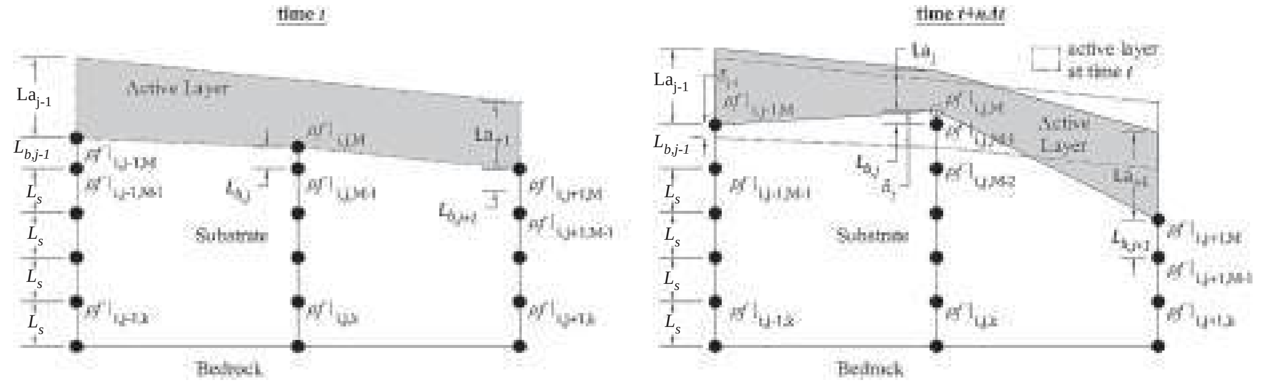

Figure 4. Representation of the stratigraphy changes for times t and $t + n\Delta t$ (where n is a large integer number). The nodes j and $j-1$ represent the two cases of aggradation with and without the creation of a new layer, respectively; and the node $j+1$ is the representation of the removal of the topmost layer for the degradation case. The subscript j denotes the nodes in the substrate at control volume j, while the subscript k represents the vertical position of nodes within the substrate.

In case of degradation, $f_{i,j,M}$ and $\rho_{si,i,j,M}$ remain constant and the elimination of vertical nodes k occur when $L_b < 0$.

2.4. Implementation in the Paraopeba River

To evaluate the impact of the presence of iron tailings along the Paraopeba River, we performed a long-term analysis assuming the bathymetric conditions measured in October 2020, which accounts for the dredging operations performed near the Ferro Carvão confluence to remove tailings from the river. A 1D sediment transport and hydraulic model was implemented along the study domain (Figure 1) to assess long-term trends in the evolution of the spatiotemporal distribution of iron tailings in the river. To estimate sediment transport rates and river morphodynamic evolution, a steady, gradually varied flow approximation, numerically solved using the secant method was implemented. This approach accounts for both subcritical and supercritical flow regimes to estimate hydraulic variables, including mean velocities, bed shear stresses, shear velocities, and water depths, at each cross-section and for every time step. The friction and local losses were included in this hydraulic analysis. The former was calculated via average conveyance between cross-sections, and the latter by the product between the head velocity difference and a loss coefficient (C) with values of 0.1 and 0.3 for contraction and expansion, respectively (i.e. $C|\alpha_{up}U_{up}^2/2g - \alpha_{dow}U_{dow}^2/2g|$).

The evolution of the bed elevation was estimated based on Equation (5). Herein, two representative diameters and densities for the iron tailings and for the ambient sand were considered. Under this simplification, it is possible to demonstrate (see derivation in Appendix A) that the rates of change $\partial L_a/\partial t$ and $\partial \rho_a/\partial t$ can be estimated as a function of the rate of change fraction of the ambient sand F_s, $\partial F_s/\partial t$ (Equations (8), (9), and (10)), as follows:

$$\frac{\partial L_a}{\partial t} = 0.3 L_a \ln(2)(\psi_s - \psi_T)\frac{\partial F_s}{\partial t} \tag{8}$$

$$\frac{\partial \rho_a}{\partial t} = \frac{\partial F_s}{\partial t}(\rho_s - \rho_T) \tag{9}$$

$$\rho_s \frac{\partial F_s}{\partial t} = \frac{1}{(1-\lambda_p)L_a}\left[-\frac{\partial g_{Ts}}{\partial x} + \frac{\rho_s f_{Is}}{\rho_I}\frac{\partial g_T}{\partial x}\right] \times \left[\frac{1}{(1+K_1)+(1+K_2)-1}\right] \tag{10}$$

where:

$$K_1 = 0.3\ln(2)(\psi_s - \psi_T)\left(F_s - f_{Is}\frac{\rho_a}{\rho_I}\right),$$

$$K_2 = -f_{Is}\frac{(\rho_s - \rho_T)}{\rho_I}$$

where ρ_T is the representative iron tailings density, ρ_s representative density of the ambient sand, $\psi_s = \log_2 D_s$, $\psi_T = \log_2 D_T$, f_{Is} is the interfacial fraction exchange for ambient sand, and F_s is the volumetric fraction of the ambient sand in the active layer.

One can demonstrate that $K_2 = 0$ if we assume $\partial \rho_a/\partial t = 0$, or that $K_1 = 0$ if $\partial L_a/\partial t = 0$. Furthermore, if both $\partial L_a/\partial t$ and $\partial \rho_a/\partial t = 0$, then K_1 and K_2 are equal to zero.

Equations (5), (8), (9) and (10) are the governing equations that are used in this study to determine the spatio-temporal evolution of the iron tailings and the riverbed elevation along the Paraopeba River. These equations were solved numerically by developing a Python code that employs a finite volume method with an explicit numerical scheme. The hydraulic variables required to solve the previous equations were estimated at each time step and all cross-sections through a steady, and gradually-varied flow approximation.

2.4.1. Sediment transport equation

One of the most widely used sediment transport equations for sand-bed rivers is the Engelund–Hansen equation (Engelund & Hansen, 1967). This single-diameter equation has been successfully tested in rivers and flumes (Garcia, 2008), and it has been extended for sediment mixtures by Naito et al. (2019) and An et al. (2020), for sand-silt and sand-bed rivers, respectively. This SEH is expressed as:

$$N_i^* = A_i(\tau_i^*)^{B_i} \tag{11}$$

with:

$$A_i = a\left(\frac{D_i}{D_{sg}}\right)^b, \quad B_i = c\left(\frac{D_i}{D_{sg}}\right)^d$$

where a, b, c and d are calibration parameters; N_i^* is the dimensionless sediment transport rate in the grain size ith range (Equation (12)); D_i is the ith grain size diameter; D_{sg} is the geometric mean size; and τ_i^* is the Shields number in the grain size ith range (Equation (13)):

$$N_i^* = \frac{C_f R g q_T f_i}{u_*^3 F_i} \tag{12}$$

$$\tau_i^* = \frac{\tau_b}{\rho g R D_i} \tag{13}$$

where f_i is the volume fraction in the ith grain size of the total bed material load; F_i is the volume fraction in the ith grain size of the active layer; u_* is the shear velocity; g is the acceleration of gravity; R denotes the submerged specific gravity of the sediment $R = (\rho_{sed} - \rho_w)/\rho_w$ (where ρ_w is the water density and ρ_{sed} is the sediment density); q_T is the volumetric sediment transport rate of total bed material per unit width; τ_b is the bed shear stress; τ_i^* is the dimensionless bed shear stress for the ith grain size; and C_f is a dimensionless bed friction coefficient.

2.4.2. Calibration of the SEH relation

The calibration parameters of the SEH equation (An et al., 2020) were determined using the dataset of Guy, Simons and Richardson collected in two recirculating flumes at the hydraulics laboratory of Colorado State University (Guy et al., 1966). As this equation was obtained for controlled laboratory conditions, we decided to calibrate the parameters for the conditions of the Paraopeba River as this river has considerable anthropogenic pressures that differ from the natural sediment regime of the river (Calazans et al., 2018; IGAM, 2010, 2013).

For the Paraopeba River analysis, we utilized two distinct datasets representing conditions before and after the accidental release of the tailings. For pre-arrival conditions, we used historical records from the Porto Mesquita streamgage (CEMIG 40865001), which provide monthly data from 1978 to 2012, including flow discharge, water temperature, grain size distribution (GSD) of both suspended sediment and bed material (Figure 5), mean velocity, hydraulic width and suspended sediment concentration (SSC). For post-arrival conditions, we relied on field measurements conducted by Vale at the locations shown in Figure 1. Both datasets were used to calibrate the SEH equation as they include a range of mixtures from pure ambient sand to pure tailings, reflecting various sand–tailings fractions and densities.

The calibration of the SEH equation for the Paraopeba River conditions is based upon the suspended sediment measurements, as the sediment measurements from the field campaigns after the accident revealed that the bedload transport rates are negligible compared with the suspended sediment loads.

The F_i values were estimated based on the GSD measurements in the bed and for fractions up to 2.0 mm, as this is the maximum size reported for the suspended material. The f_i values were calculated based on the common diameters found both in the bed and in suspension, as these diameters are responsible for the morphologic changes in the river. The GSDs for this condition were obtained by renormalizing the GSD of the bed material for sizes between the washload diameter to a diameter of 2.0 mm. Following the methodology proposed by An et al. (2020), the renormalized curves were fitted to the cumulative distribution function (CDF), assuming that they satisfy a Gaussian distribution (see red lines in Figure 5). For this analysis, values of $f_i < 0.005$ were discarded because the lognormal distribution becomes less applicable for extremely small values. This issue arises because the finest and coarsest tails of the grain size distribution (GSD) are not well-represented by the lognormal distribution. This distribution is often used to model GSDs because it tends to fit well with the bulk of the data, particularly for medium-sized grains. Sediment grain sizes, often exhibit a skewed distribution where most grains fall within a certain size range, with fewer grains in the very fine or very coarse categories. The lognormal distribution is effective in capturing this skewness for most of the distribution. However, the tails of the distribution, representing the finest and coarsest grains, might not be as well captured by a lognormal distribution. In these regions, the actual grain size distribution might deviate from the lognormal assumption, leading to inaccuracies.

The submerged specific gravity (R) plays an essential role in this calibration as it allows us to determine the presence of tailings in the sediment bed. For pre-accident conditions, a bed density of 2650 kg m^{-3} was assumed for all sediment records at the Porto Mesquita streamgage. For the remaining sediment measurement sites, we used the R measured at these sites. The friction slopes at all sites were estimated by performing a 1D-hydraulic analysis in a steady-state condition and considering the hydraulic measurements and the cross-section surveys conducted during the field campaigns.

The calibration of the SEH is based on Equations (11) and (12), which, in this case, represent

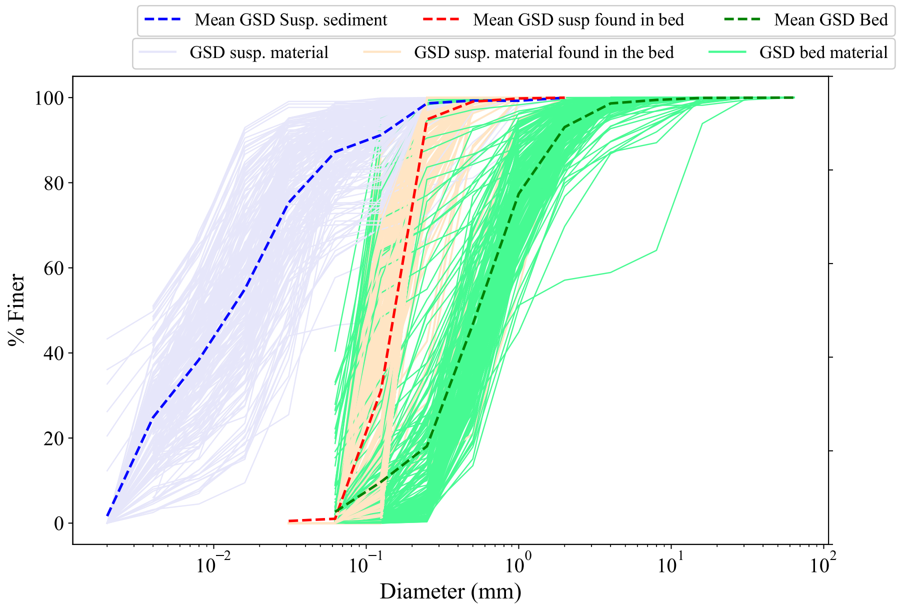

Figure 5. GSD for bed material, suspended sediment and suspended sediment that is found in the bed. Dash lines are the mean GSD.

the simulated and the observed data, respectively. The calibration parameters were determined via the shuffled complex evolution (SCE-UA) method (Duan et al., 1992) as is an efficient and global optimization algorithm that is widely used for calibrating conceptual models (Muttil & Jayawardena, 2008; Vrugt et al., 2003). Each set of parameters was evaluated according to an objective function. In this case, the best set of parameters was obtained by minimizing the Kling–Gupta efficiency equation (KGE, Equation (14), Gupta et al., 2009). A perfect agreement is reached when KGE = 1 or 1−KGE = 0. As the observed data span over four orders of magnitude, different transformations were evaluated (e.g. square root, inverse, logarithm) before estimating the objective function (1−KGE) to give more prominence to low values. For this case, the logarithmic transformation was selected as it led to the greatest minimization of the objective function and also the measured values differ from zero:

$$\mathrm{KGE} = 1 - \sqrt{(r-1)^2 + \left(\frac{\sigma_{sim}}{\sigma_{obs}} - 1\right)^2 + \left(\frac{\mu_{sim}}{\mu_{obs}} - 1\right)^2} \tag{14}$$

where r is the Pearson correlation coefficient between observed and simulated data; σ_{sim} and σ_{obs} are the standard deviation of the simulated and observed data, respectively; and μ_{sim} and μ_{obs} are the mean values of the simulated and observed data, respectively.

The calibrated parameters obtained via SCE-UA were $a = 0.0323$, $b = -1.466$, $c = 1.603$ and $d = 0.094$. These parameters minimize the objective function, resulting in 1−KGE = 0.59. Similar calibrated parameters and objective function values were obtained when using other methods such as cuckoo search algorithm (X. S. Yang & Deb, 2009), sequential least squares programming (Kraft, 1988), and 'brute force' with uniform distribution (Appendix 4).

Although there is a considerable dispersion between the observed and predicted N_i^* and q_i^* values, the calibration performed via the SCE-UA method is relatively accurate in representing the observed data (Figure 6). A complementary analysis about the reasons for the dispersion of the data and a comparison with the original SEH equation proposed by An et al. (2020) can be found in Appendix 4.

2.4.3. Boundary conditions

To study the long-term evolution of the iron tailings in the river, we used a constant dominant discharge that herein refers to a steady flow condition that would transport the mean total sediment load if kept constant over time (Appendix 3 outlines the methodology for the estimation of the dominant discharge). A constant flow rate of 116.9 m^3 s^{-1} and a mean annual sediment load of 0.21 Mton day^{-1} are the upstream boundary conditions estimated based on the historical flow rates records from the streamgage Alberto Flores (4074000) and the sediment measurements taken at site P0 (Figure 1). At the downstream end, we set a water surface elevation equal to 616.0 m, which is the maximum normal water elevation in the Retiro Baixo Reservoir (Soares Sobrinho & Graça, 2009). We could have chosen as the downstream boundary condition any value between the minimal operational elevation (602.3 m) and the maximum operational elevation (617 m) in the reservoir, without having any influence on the hydraulic results along the river for the dominant discharge condition. This is due to the significant control exerted by bedrock outcrops, particularly near the headwaters of the Retiro Baixo Reservoir, as indicated

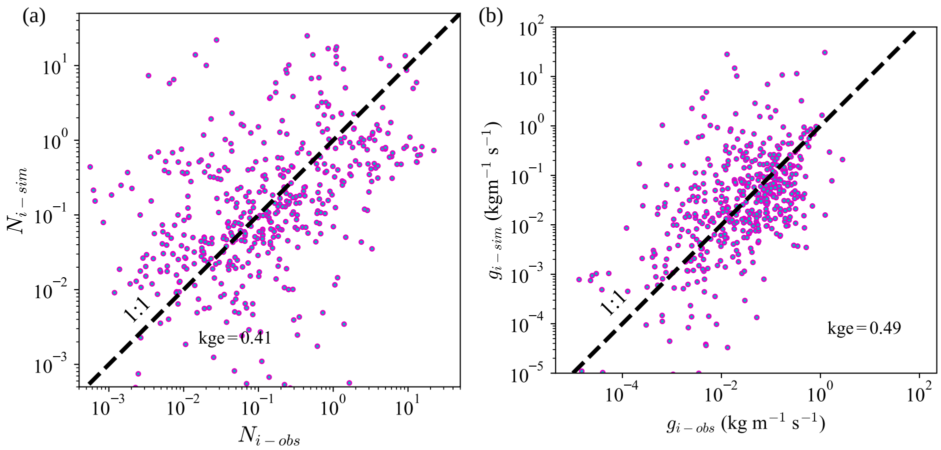

Figure 6. Comparison between observed and simulated values. (a) Dimensionless sediment transport rate N_i; (b) dimensionless sediment transport rate per unit width for the diameter in the ith range size, q_i.

Table 1. Flow discharges used in the hydraulic and sediment transport model.

Reach	Q (m^3 s^{-1})
Melo Franco (−10 km) – Confluence Betim River (+45.8 km)	116.9
Confluence Betim River (+45.8 km) – Confluence Macacos Creek (+177.8 km)	165.9
Confluence Macacos Creek (+177.8 km) – Porto Mesquita (+241.0 km)	200.0
Porto Mesquita (+241.0 km) – upstream Retiro Baixo Reservoir (+295.0 km)	205.5

Note: Positive sign corresponds to distances downstream of the Ferro Carvão confluence, while negative sign refers to upstream distances.

in the longitudinal profile from the spillway at Igarapé to the Retiro Baixo Reservoir (Figure A5).

The contribution of the tributaries were considered by dividing the domain in four different subreaches. A constant flow rate was assigned at each subreach based on the dominant discharges at the upstream end of each subreach (Table 1), according to the streamgage records and the drainage area at each subreach. Based on the historical records reported at the streamgages, the mean annual sediment loads remained constant for the entire domain, for the conditions before the accident. This might be due to the dammed tributaries, the dredging operations along the river, and the presence of hydraulic structures (i.e. spillways). Therefore, for the purposes of analysing dominant discharge conditions, the sediment input from the tributaries can be considered negligible (mean annual sediment loads along the river are in the order of 0.2 year^{-1}, Table A2).

2.4.4. Model geometry

In this modelling effort, the river geometry was simplified by adopting a rectangular cross-section with varying widths. These widths were derived from a 1D steady-state hydraulic analysis, based on a fixed-bed assumption and real cross-sections obtained from a bathymetric survey conducted in October 2020. The hydraulic analysis accounted for both subcritical and supercritical flow regimes and the hydraulic variables were determined numerically using the secant method.

The simplified rectangular cross-section, with its variable widths, was implemented in the movable-bed model to determine the spatio-temporal evolution of the riverbed and the transport of iron tailings along the river. We did not consider floodplains because, in the upper part of the domain, the river flows through a valley with mild slopes where floodplains are limited. Although there are floodplains in the lower course, the dominant discharge stages were lower than the bankfull stages.

Due to the high variability in both bathymetry and sediment composition near the confluence, we selected a finer cell size (dx) of 40 m in this area to capture detailed changes accurately. For regions extending 6 km downstream to the Igarapé spillway, we opted for a cell size of 350 m, anticipating moderate changes in river morphology and sediment composition. For the reach downstream of the Igarapé spillway, we selected a dx of 500 m, as the bathymetry in that reach is represented by cross-sections spaced 1 to 2 km apart, and the bathymetric surveys and sediment measurements indicate that this subreach is less likely to be significantly affected due to the presence of the spillway at Igarapé. Additional cells were defined at bedrock rapids and at the spillway at Igarapé as vertical erosion is controlled at these locations.

The time step chosen for the morphological calculation Δt was based on the stability of the numerical scheme and the maximum erosion or aggradation allowed in each time step. For this analysis, the maximum erosion allowed in one time step was set to be equal to the substrate layer thickness ($L_s = 0.20$ m). We also ensure that there are no numerical instabilities at the flow discharge transitions across the various subreaches, which could otherwise result in severe bed scouring. For the following months after the accident, we used 0.5 min as the time step, as the sediment was moving relatively fast at locations close to the Ferro

Carvão confluence. As the river morphology and sediment fractions approached equilibrium, we progressively increased the time step. In these more stable conditions, we utilized a time step of 30 min.

2.4.5. Hydraulic and sediment parameters

The C_f values were estimated based on the resistance relations expressed in terms of power laws and on the composite roughness k_c, which includes the effect of the grain friction and form drag (Equation (15)):

$$C_f = \left[\left(\frac{R_h}{k_c}\right)^{1/6}\right]^{-2} \tag{15}$$

where C_f is the friction coefficient, and R_h is the hydraulic radius.

For the first iteration, the k_c is estimated based on the calibrated Manning's n_c values that were estimated assuming fixed-bed conditions along the river (Vale & Potamos, 2020). In the subsequent iterations, these values are updated as the hydraulic and sediment conditions change.

We selected two representative diameters that represent the natural sediment and the iron tailings in the river assuming a porosity equal to 0.35. The characterization of the measurements along the river shows that the natural bed material is mainly medium sand with a D_{sg} around 0.35 mm. For the iron tailings, we chose a diameter of 0.10 mm that is based on the measurements taken inside the Córrego do Feijão Dam-I before the accident (Figure 7). The density measurements right after the accident show measured density values up to 5000 kg m^{-3}. However, a mineralogical analysis performed with core samples along the river reported that density values of iron tailings range between 3200 to 4500 kg m^{-3}, while the natural sediment values range from 2570 to 3550 kg m^{-3} (Arcadis & Vale, 2021; Laureano et al., 2022). Herein we considered two representative densities: 2810 kg m^{-3} and 3960 kg m^{-3} for the natural sediment and the iron tailings, respectively. For the natural sand, we selected 62.5 μm as the cut-off size for the wash load material and 48.5 μm for the iron tailings. The latter value is estimated as the equivalent grain size with $R = 2.96$ that gives the same fall velocity estimated for the cut-off size for the natural sand.

The bed sediment measurements taken upstream of the Ferro Carvão confluence show that the wash load component is negligible. However, the bed measurements collected at P1, in March 2019, show a considerable amount of tailings that include diameters within the wash load sizes. As this paper aims to study the mixing and bed evolution of the iron tailings material, we removed the wash load fraction of the tailings as this material is transported in the water column and would not have a significant influence on the morphological changes of the river.

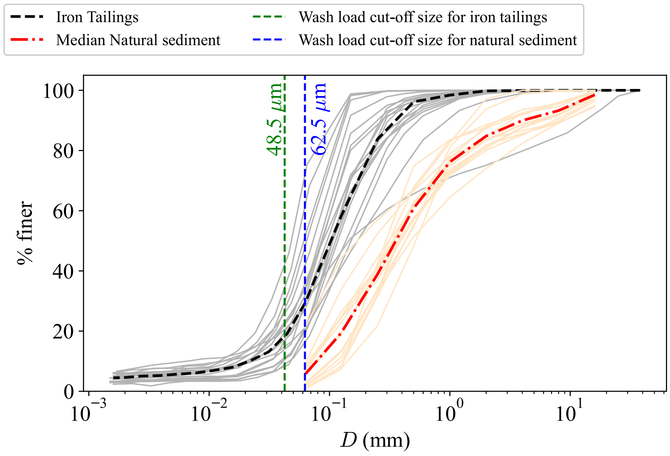

Figure 7. GSDs of tailings and natural bed sediment measured at site P0 along with the wash load cut-off sizes for tailings and natural sand. Grey curves represent the GSD measurements at Dam-I before the accident, while bisque curves are the bed measurements taken at P0.

2.4.6. Active layer thickness and bedforms

The thickness of the active layer is difficult to define; however, it is common to assume that it scales with the geometry of bedforms or the water depth (Karim & Kennedy, 1982; Rahuel et al., 1989; Wright & Parker, 2005). Although no bedforms were measured during the field campaigns, dunes, ripples, and flatbeds are expected according to the Shields–Vanoni–Parker river diagram (Garcia, 2008; Parker, 2004) shown in Figure 8. These predictors suggest that dunes are the predominant bedform along the river; however, ripples and flatbed are expected at locations close to the confluence with the Ferro Carvão Creek (P1 and P2), as the sediment–tailings mixture is smaller and denser than the natural sediment.

Bedrock outcrops have been identified at a few locations with drastic elevation drops that lead to local flow acceleration and erosion control. When the bedrock is exposed, the development of bedforms is unfeasible, and the numerical model treatment allows the sediment material to bypass the cell, impeding any erosion (only deposition). The sediment transport capacity at this cell does not consider the surrounding cells to avoid any instability propagation due to bedrock exposure. For cases without bedrock exposure, it is assumed that the thickness of the active layer scales with the dune height according to Equation (16) (Julien & Klaassen, 1995):

$$L_a = \alpha_D \Delta_{dune} = \alpha_D \left[\xi H \left(\frac{D_{sg}}{H}\right)^{0.3}\right] \tag{16}$$

where H is the water depth, α_D is a constant that ranges between 0.4 and 8.0, Δ_{dune} denotes the dune height; and ξ is a constant that ranges between 0.8 and 8.0.

2.4.7. Initial conditions

The initial bed elevations along the study domain are based on the thalweg of the river according to the

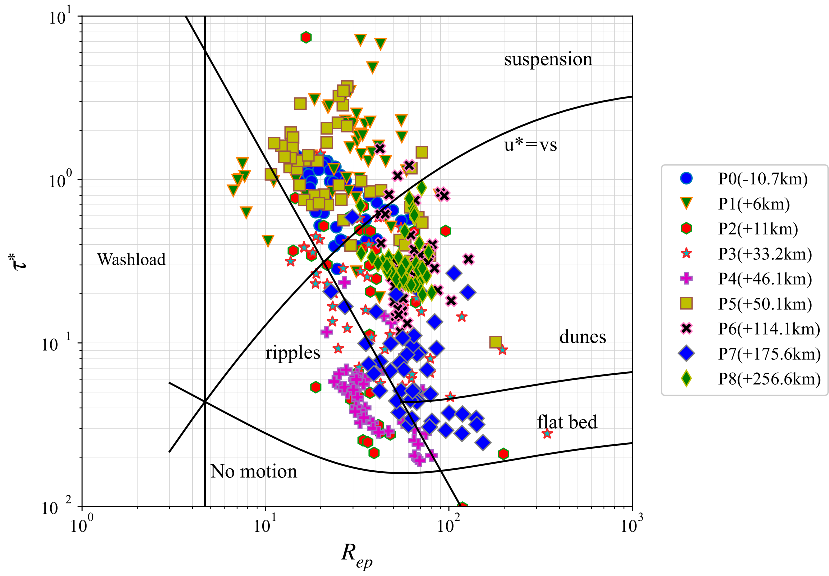

Figure 8. Bedforms expected at measurement sites along the Paraopeba River according to Shields-Vanoni-Parker diagram (Garcia, 2008; Parker, 2004). Positive sign indicates distance downstream the confluence with the Ferro Carvão Creek while negative sign indicates distance upstream the confluence.

bathymetry obtained in October 2020, which indirectly includes the dredging operations performed in the surroundings of the Ferro Carvão confluence. The initial density and volume fractions at each cross-section must be defined at the active layer and at all nodes within the substrate. As some of the mining material has been transported downstream, we use the bed measurements to determine the bulk densities in the active layer as initial conditions for our simulations. The densities along the river are determined by linear interpolation based on the values at the measurement sites, except in the first 6 km, where we assume that the bed is covered with iron tailings (i.e. $F_T = 1$, $F_s = 0$).

The initial conditions in the substrate were based on the core sampling and bathymetries along the first 6 km. Based on these measurements, Vale and Saga (2021) constructed a 3D solid representation to approximately determine the thickness of the tailings material, the natural sand, and the saprolite. We used this thickness to determine the sand and sediment fractions within the substrate for this first 6 km. The substrate elsewhere was assumed to be composed mainly of sand (i.e. $F_T = 0$, $F_s = 1$). A schematic profile of the initial conditions for the subreach between the confluence of the Ferro Carvão Creek to the spillway next to the Igarapé Power Plant is represented in Figure 9.

3. Results and discussion

The results described in this section are for a long-term condition in which the density and bed evolution of the sediment bed are simulated for a representative flow discharge condition that would transport the annual sediment load (i.e. dominant discharge). Therefore, we are not trying to represent the historical conditions as the flow discharges are a function of the hydrology of the basin and the water releases from reservoirs located in tributaries of the Paraopeba River.

3.1. SEH equation

Since the iron-ore tailings are finer than the ambient sediment, their presence temporarily makes the grain size distribution (GSD) of the riverbed finer and more uniform. This results in the bed material being transported in suspension becoming finer than the suspended material before the arrival of the tailings. Depending on the presence of iron tailings, this condition can lead to a fining effect, resembling the characteristics of a silt-bed river (e.g. Yellow River, China). The observed data (collected at all sediment measurement locations along the Paraopeba River, Figure 1) clearly demonstrates this fining trend, which shows a riverbed fining as the dimensionless shear stress increases (Figure 10). According to Naito et al. (2019), this behaviour contrasts with what is typically observed in gravel-bed rivers.

For rivers like the Yellow River, the exponents b and d are negative due to the fining of the suspended load (Naito et al., 2019). Although a fining effect is occurring in the Paraopeba River, it will not fully reach the condition of a silt-bed river. However, this fining effect causes the coefficient b to become negative, while d becomes positive, albeit very close to zero. Overall, this condition results in higher N_i^* values using the model developed here compared to those calculated using the formula of An et al. (2020) (Figure A2a). Consequently, this leads to increased suspended sediment transport rates due to the high entrainment rates into the water column caused by the fining effect of the riverbed (Figure A2b).

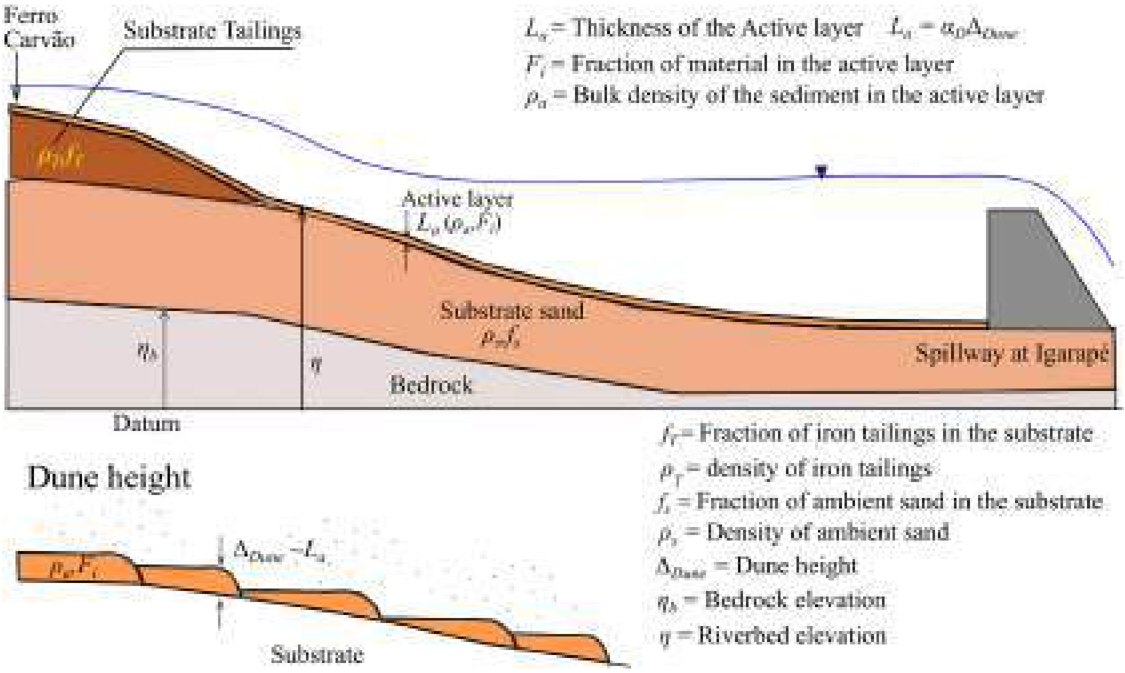

Figure 9. Schematic profile that represent the initial conditions for the reach between Ferro Carvão to the spillway at Igarapé Power Station.

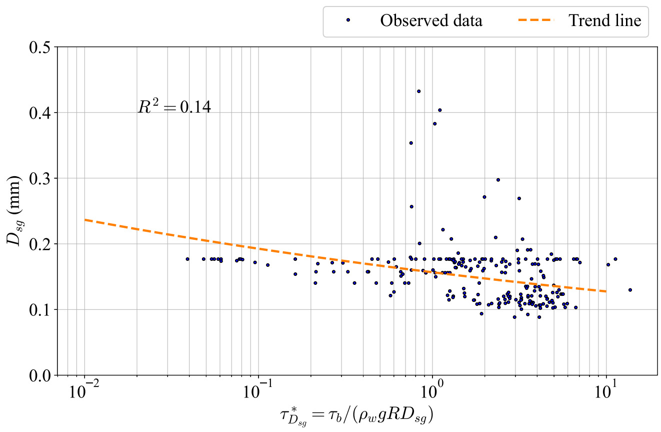

Figure 10. Dimensionless shear stress versus geometric mean grain size.

3.2. Bed evolution

As bedrock outcrops vertically control the erosion in the Paraopeba River, the current analysis focuses on the Ferro Carvão Creek confluence, as this zone is prone to erosion due to the volume of tailings that were deposited in this area after the dam breach incident. Likewise, this analysis focuses on the pool upstream of the spillway at the Igarapé Power Plant, as the eroded and mobilized iron tailings tend to be temporarily deposited in low-velocity zones.

The simulation results show a rapid erosion of the iron tailings for the first years at the Ferro Carvão Creek confluence, with relatively constant and almost imperceptible changes after the fifth year (Figure 11a). On the other hand, the pool upstream of the Igarapé spillway is prone for the tailings to deposit as low flow velocities are induced by the backwater curve generated by this structure. After the pool is filled with the sand–tailings mixture, minor changes are expected in the bed elevations along the pool (Figures 11b). The sediment–tailings mixture enters this slowly moving zone that decreases the ability of the river to move sediment at the same rate that was moving upstream of the pool. It is expected that the sand–tailings mixture would be maintained upstream of the spillway until this mixture reaches its crest in approximately 17 years. This is only an approximate estimate since the dominant discharge is used and not the actual flow discharge conditions.

This bed evolution analysis does not aim to capture the actual changes of the bathymetry because the real bed evolution is a function of the flow discharges conveyed by the river and the dredging operations that are conducted in the zone adjacent to the Ferro Carvão confluence. These variable flow discharges differ from the constant flow dominant discharge; thus, we would not expect to reproduce the observed bed evolution. Herein we are considering a virtual flow discharge (flow dominant discharge) that would provide the mean annual sediment load in the long term. In the same manner, although we consider the effects of dredging operations by using a bathymetry performed in October 2020 (20 months after the accident), we cannot consider subsequent dredging operations in the current analysis.

The evolution of the rating curves at the Alberto Flores streamgage (Figure 12), located 1 km upstream of the Ferro Carvão confluence, shows evidence of the rapid erosion predicted in the simulation results and

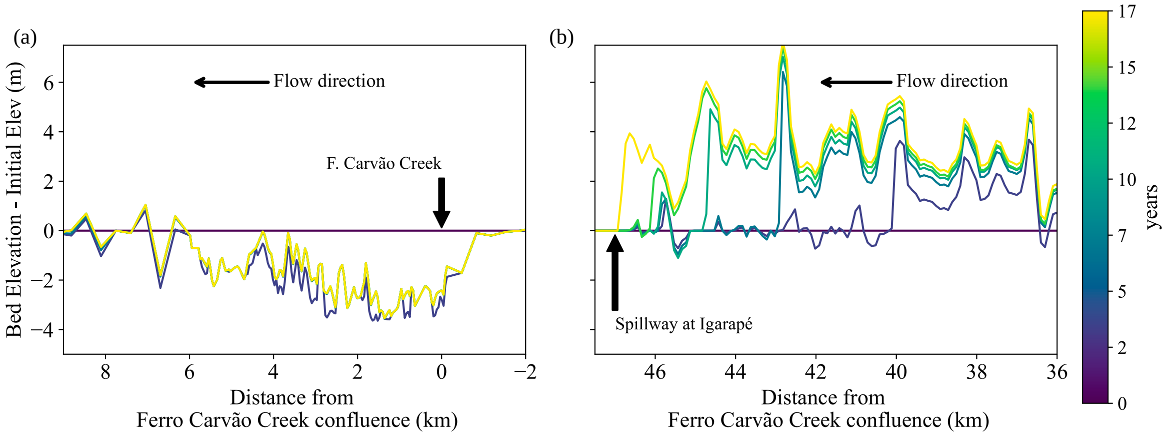

Figure 11. Relative bed changes based on initial bed elevation (bathymetry October 2020). Negative numbers indicate erosion while positive ones correspond to aggradation. (a) Ferro Carvão confluence. (b) Igarapé Pool.

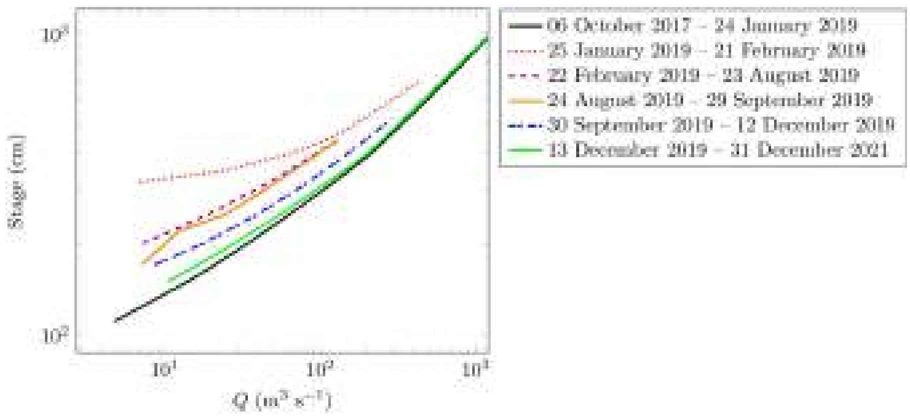

Figure 12. Evolution of the rating curves before and after the accident at streamgage Alberto Flores (ANA 4074000). Note: this figure is based on data reported by ANA (Agência Nacional de Águas, Brazilian Water Agency) at this streamgage.

the survey bathymetries performed after the arrival of the iron-ore tailings (Figure 11). This erosion plus the dredging operations conducted in this zone have almost restored the hydraulic conditions in this area of the river, as the rating curve measured by ANA in December 2021 (green line) is close to the one measured before the dam breach (black line).

The rating curves measured after the accident show a rapid increase of the water surface elevations in the river (at Alberto Flores streamgage) due to the large deposit of iron tailings formed after the dam breach. This tailings deposit blocked the river flow and created a backwater curve extending up to the Almorreimas Cascades, located 1.7 km upstream of the Ferro Carvão confluence (Figure A4). The multiple topographic surveys and the simulation results demonstrate that once the river passes over this mound, the flow accelerates due to the steep longitudinal slopes, easing the entrainment of this material into the water column and rapidly eroding the tailings mound. This continuous erosion and the dredging operations decrease the longitudinal slopes of the iron tailings deposit and, thus, the sediment transport capacity of the river. The restoration of the hydraulic conditions at the Alberto Flores streamgage was achieved in less than one year (Figure 12), despite the considerable volume of iron tailings that remain in the bed according to the core sampling performed in the first 6 km downstream of the Ferro Carvão Creek confluence (Vale & Saga, 2021). This rapid hydraulic restoration was achieved due to the pool-riffle sequence of the Paraopeba River, in which the hydraulic conditions at the Alberto Flores streamgage are controlled mainly by a riffle located upstream of the Ferro Carvão confluence (Figure A4).

To provide an explanation for the predicted rapid erosion of this material within the first 6 km, we conducted an analysis of the entrainment of this non-fluvial material from the bed to the water column. Although the simulation results and the topographic surveys indicate a high mobility of the iron tailings in the downstream direction, it is crucial to consider that the sizes of this non-fluvial material are finer than riverbed material and comparable with the thickness of the viscous sublayer. Therefore, the iron-ore tailings can be totally or partially immersed into this sublayer requiring high turbulence intensities and bottom shear stresses to be entrained into suspension (Rojas-Aguirre & Garcia, 2025). To determine the flow conditions conducive to entrainment, we used the bathymetry survey conducted in September 2021, as it includes a stratigraphic

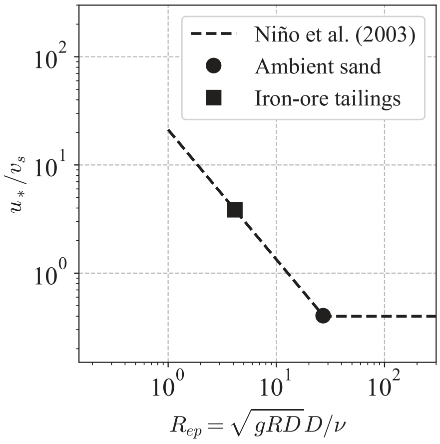

Figure 13. Threshold for entrainment for the tailings and ambient sand assuming representative diameters.

analysis based on core sampling taken for the first 6 km downstream of the Ferro Carvão confluence (Vale & Saga, 2021).

According to Nino et al. (2003), the threshold that triggers the entrainment of sediment from the bed into suspension is a function of the Reynolds particle number, R_{ep} (Figure 13). For the representative diameter for the iron tailings (i.e. $D = 0.10$ mm), the flow in the river must be capable of reaching values of at least $u_*/v_s = 2.81$ to entrain the tailings into the water column. This threshold is higher than the one obtained for the natural sand ($u_*/v_s = 0.40$), leading to a condition in which higher turbulence intensities are required for the representative tailings diameter to be entrained in comparison with the ones required for the representative diameter of natural sand.

Based on the formulation proposed by Nino et al. (2003) and a steady-state hydraulic analysis assuming fixed-bed conditions, it was found that for the first 6 km downstream of the Ferro Carvão Creek confluence, the river has enough capacity to entrain the iron tailings into the water column, regardless of the streamflow magnitude (i.e. flow equal to or exceeded 95% of the time, the mean flow discharge, and dominant flow discharge). The majority of the u_*/v_s values surpass the threshold for tailings entrainment which can be observed in the dashed red line depicted in Figure 14c. During low streamflows, we can expect high entrainment in the riffles zones as the flow tends to go to a critical regime leading to high magnitudes of u_*/v_s. On the other hand, deposition is expected in pool zones as the values of u_*/v_s are lower than the threshold for entrainment of tailings.

3.3. Density and size evolution

As the sediment density is our surrogate to track the transport and dispersion of the iron tailings in the river, we evaluate the spatiotemporal evolution of the bulk density in the active layer, as we assumed that the material within this layer interacts with the

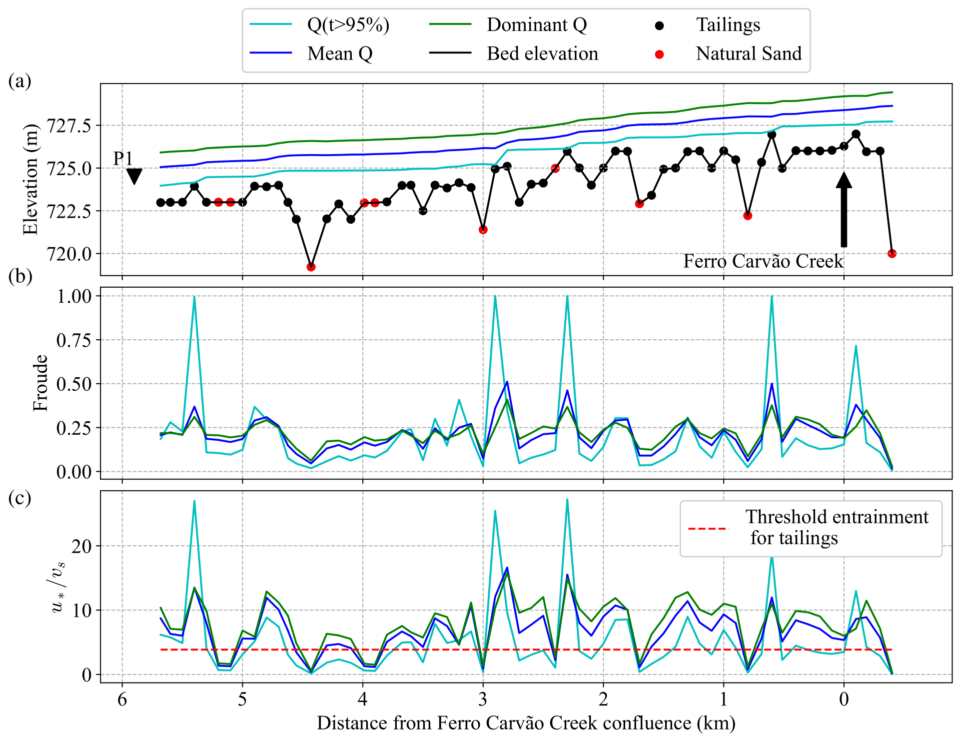

Figure 14. Analysis for entrainment of tailings in the first 6 km downstream the Ferro Carvão Creek. We considered three flows: the flow equal to or exceeded 95% of the time according to the records at streamgage Alberto Flores (16.7 m^3 s^{-1}), the mean flow discharge (61.4 m^3 s^{-1}), and the dominant flow discharge (116.9 m^3 s^{-1}). (a) Water surface elevations and bed profile for bathymetry 2021. (b) Froude number. (c) u_*/v_s along with the threshold for entrainment of tailings into suspension.

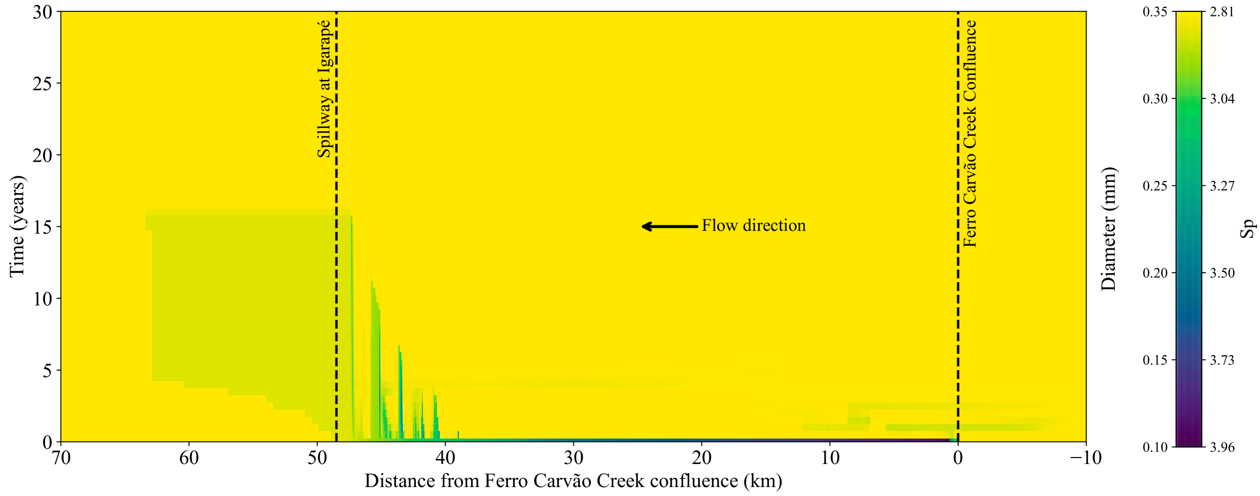

Figure 15. Spatio-temporal evolution of mean geometry size D_{sg} and specific gravity ($S_p = \rho_s/\rho_w$) within the active layer. Pure tailings and pure sand are represented with S_p of 3.96 and 2.81, respectively, while the mixture of these materials has S_p that fall within this range.

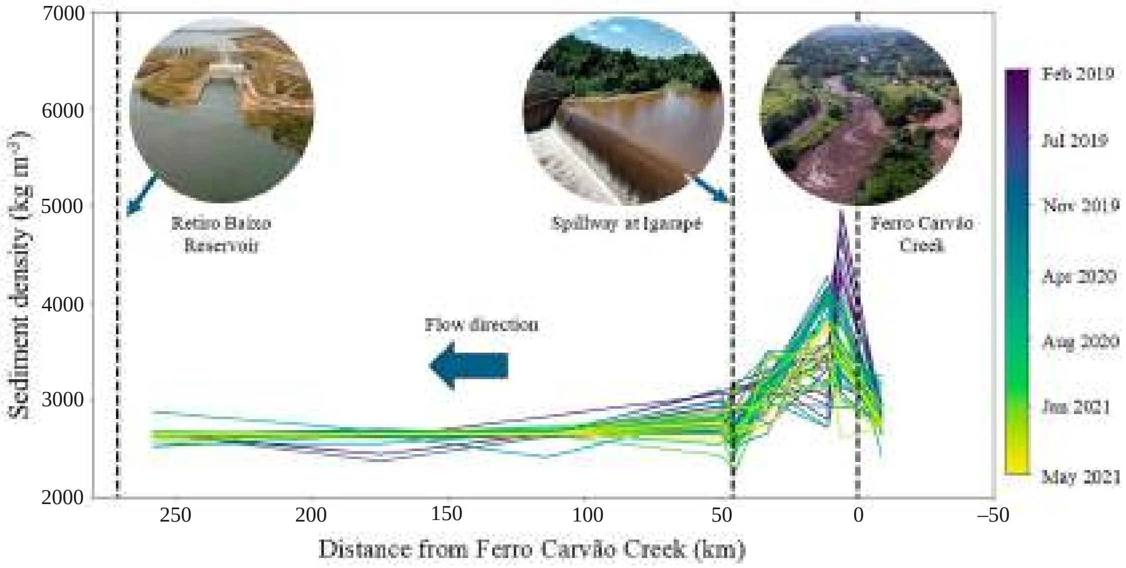

Figure 16. Spatio-temporal evolution of the density of the riverbed material based on observed data. Note: this figure was created using the dataset from field sediment campaigns conducted by Vale at the ten measurement locations depicted in Figure 1.

water column and is prone to move in the downstream direction.

Figure 15 represents the spreading of the mixture of sand–iron tailings along the river, based on the evolution of the sediment density and geometric diameter within the active layer. The iron tailings in the active layer rapidly interact and mix with the natural sediment material, in the reach from the Ferro Carvão confluence to upstream of the spillway. Although we are not aiming to represent the historical conditions in the river, the simulation results are consistent with the general pattern of the spatiotemporal evolution of the density of the riverbed material measured at the sediment measurement locations. This suggests a high level of dissipation of iron tailings discharged into the river, primarily due to their mixing with ambient sand and the burial of some material within the substrate. Furthermore, a significant portion of the non-washload component of the iron tailings remains trapped upstream of the spillway at Igarapé (Figure 16), which aligns with the findings of previous studies by Salgado Terêncio et al. (2023).

The long-term simulation results of the riverbed sizes and density evolution along the pool upstream of the spillway predicts a change in its stratigraphy caused by the backwater effects developed by the structure (Figure 17). The low velocities in this zone imply low bed shear stresses that decelerate the sediment transport rates compared to other river zones. The simulated stratigraphy analysis along the pool predicts that fractions of iron tailings would be buried, and a downstream lightening process (Viparelli et al., 2015) would occur since the denser materials would remain in the pool and the lighter sediment (i.e. with low

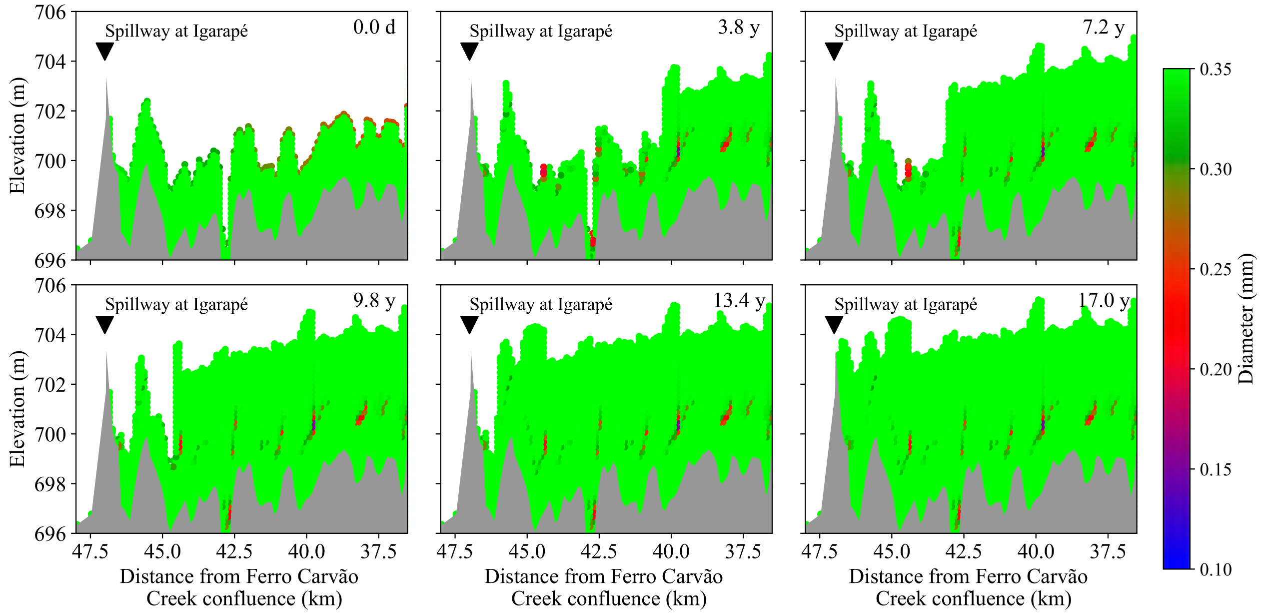

Figure 17. Evolution of D_{sg} in the substrate in the pool upstream of the spillway at Igarapé. The flow direction is towards the left.

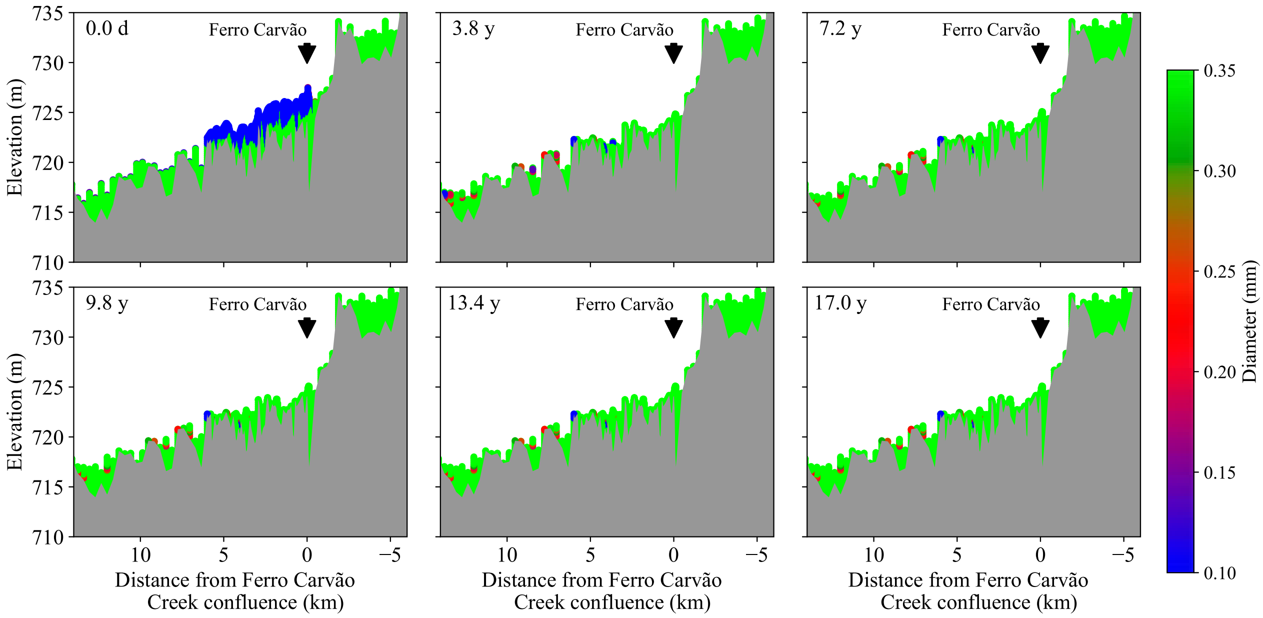

Figure 18. Evolution of D_{sg} in the substrate in close to the Ferro Carvão confluence. The flow direction is towards the left.

iron content) would reach the crest of the spillway. Therefore, the pool upstream of the spillway acts as a settling tank controlling the spreading of the coarse iron tailings downstream of the structure. Due to the substantial accumulation of material upstream of the structure, simulations indicate that the sediment passing through it would consist of less than 5% iron tailings by volume (i.e. 95% sand). At distances beyond 63 km downstream of the Ferro Carvão Creek confluence, the presence of these tailings would be nearly undetectable.

Despite the previous result, this trapping effect upstream of the spillway might differ from what is expected to occur in large streamflow events. Given the high propensity of tailings to be entrained into the water column, large events would have the potential to move the sand–tailings mixture beyond the spillway at Igarapé. Thus, to provide a more accurate representation of sediment movement in this low-velocity zone, we recommend implementing a depth-averaged sediment conservation equation for suspended sediment in future studies. Additionally, instead of estimating sediment transport using a total sediment transport equation, we suggest adopting a suspended sediment transport equation, as bed load rates are negligible compared to suspended sediment loads. This equation would specifically account for the entrainment of iron tailings into the water column. We also recommend conducting suspended sediment measurements throughout the water column using acoustic or optical devices to analyse the vertical distribution of concentration and particle size (Pedocchi & García, 2006).

On the other hand, the sediment bed evolution at the zone close to the Ferro Carvão Creek shows a rapid bed erosion of the iron tailings that is reflected in an increase in the mean sediment diameters in the substrate and in the riverbed (i.e. decrease in the specific gravity) due to the rapid mobility of the iron-tailings in the downstream direction (Figure 18). Although some vestiges of the tailings tend to be trapped in lower layers within the substrate, most of the eroded material is transported in the downstream direction and deposited in low-velocity zones.

Future efforts to improve the accuracy of previous simulation results involve incorporating more size fractions of the sand–tailings mixture in the numerical model. This is particularly crucial due to the heterogeneous size of the iron tailings that were accidentally released in the Paraopeba River. This size heterogeneity might cause particles to move at different velocities based on their size. Small particles are carried further downstream than the heavier ones , producing a downstream fining effect (Blom et al., 2016; Paola et al., 1992; Wright & Parker, 2005).

4. Conclusions

In this study, formulations based on the active layer concept are proposed to assess watercourses that receive material with densities differing from those of the ambient sediment. Using these formulations and a recalibrated SEH equation that accounts for varying sediment sizes and densities, we developed a 1D hydraulic and sediment transport numerical model for the Paraopeba River (Brazil). This model assesses the long-term stratigraphic and morphodynamic evolution caused by a single iron tailings pulse accidentally released into the river. By assuming a dominant flow discharge (i.e. a virtual flow capable of transporting the mean sediment load of the river over a year), we determined the long-term evolution of the pulse of iron-ore tailings along the river. Sediment density was used as a surrogate to track this material within the active layer and substrate, enabling us to capture its dispersion and fate along the river.

The results from the numerical model show that the evolution of the material density in the active layer aligns with the overall trend of observed density measurements in the riverbed. This suggest that a significant portion of the non-washload component of the iron tailings has not moved further downstream of the spillway at Igarapé (Figure 16). Consequently, the pool upstream of the spillway at Igarapé offers a suitable location to effectively monitor and control the spreading of the iron tailings in the streamwise direction, as this structure acts as a hydraulic control section in the river by creating a backwater curve and enhancing deposition.

Overall the proposed model is also able to explain the rapid bed evolution seen in the zone close to the Ferro Carvão confluence. The entrainment analysis performed in the area close to the tailings source reveals that the iron tailings are constantly in motion as the river has enough capacity to entrain them into the water column since the entrainment threshold is easily surpassed, regardless of the magnitude of the streamflow.

Acknowledgments

We would like to thank Joel Cortez, Fernando Verassani Laureano, and Vitor Pimenta, all from Vale S.A., for their collaboration. We also extend our gratitude to Prof. Enrica Viparelli and the three anonymous reviewers for their valuable suggestions, which greatly improved the quality of this paper. Finally, we are grateful to Dongchen Wang and Zhi Li for their recommendations, which significantly enhanced our numerical model.

Disclosure statement

The analysis, opinions and results presented above are solely those of the authors and are not those of any institution and/or company mentioned in the manuscript.

Funding

This work was conducted under an agreement between Prof. Marcelo H. Garcia and Vale S.A., with additional support from the M.T. Geoffrey Yeh Chair in Civil Engineering at the University of Illinois.

Notation

a,b,c,d	calibration parameters for SEH equation (–)
C_f	dimensionless bed friction coefficient (–)
D_i	sediment size in the ith grain size (m)
D_{sg}	geometric mean size (m)
f_i	volume fraction in the ith grain size in the substrate (–)
f_s	volume fraction of the ambient sand in the substrate (–)
f_T	volume fraction of the iron-ore tailings in the substrate (–)
f_{Ii}	interfacial exchange fraction in the ith grain size (–)
f_{Is}	interfacial exchange fraction of the ambient sand (–)
f_{IT}	interfacial exchange fraction of the iron-ore tailings (–)
F_i	volume fraction in the ith grain size in the active layer (–)
F_s	volume fraction of the ambient sand in the active layer (–)
F_T	volume fraction of the iron-ore tailings in the active layer (–)
g	acceleration of gravity (m s^{-2})

g_T total mass transport rate per unit width (kg m^{-1} s^{-1})
g_{Ti} total mass transport rate per unit width for ith grain size (kg m^{-1} s^{-1})
H water depth (m)
k_c composite roughness (m)
L_a active layer thickness (m)
N_i^* dimensionless sediment transport rate in the ith grain size (–)
q_T volumetric sediment transport rate of total bed material per unit width (m^2 s^{-1})
R submerged specific gravity of the sediment (–)
R_h hydraulic Radius (m)
R_{ep} Reynolds particle number (–)
u_* shear velocity (m s^{-1})
t time (s)
v_s settling velocity (m s^{-1})
x streamwise direction coordinate (–)
α_D weighting factor to estimate the active layer thickness (–)
Δt time step (s)
Δ_{dune} dune height (m)
λ_p sediment porosity (–)
ρ_a bulk density in the active layer (kg m^{-3})
ρ_I bulk density at the interface substrate-active layer (kg m^{-3})
ρ_i density in the active later in the ith grain size (kg m^{-3})
ρ_s ambient sand density (kg m^{-3})
ρ_T iron-ore tailings density (kg m^{-3})
ρ_w water density (kg m^{-3})
ρ_{Iifli} interfacial density exchange in the ith fraction (kg m^{-3})
S_p specific gravity (–)
τ_b bed shear stress (kg m^{-1} s^{-2})
τ_i^* dimensionless bed shear stress in the ith grain size (–)

ORCID

Andrés F. Rojas-Aguirre http://orcid.org/0009-0006-9085-2881
Marcelo H. Garcia http://orcid.org/0000-0003-0643-489X

References

An, C., Gong, Z., Naito, K., Parker, G., Hassan, M. A., Ma, H., & Fu, X. (2020). Grain size-specific engelund-hansen type relation for bed material load in sand-bed rivers, with application to the Mississippi River. *Water Resources Research*, *57*, 1–25.

Arcadis and Vale (2021). *Dispersão de Rejeitos na Carga de Fundo do Rio Paraopeba após o Rompimento da Barragem B1, 2a Campanha (2020)* (Technical Report 2020). Brumadinho, Brazil. (in Portuguese).

Berenbrock, C., & Tranmer, A. W. (2008). *Simulation of Flow, Sediment Transport, and Sediment Mobility of the Lower Coeur d' Alene River, Idaho*. U.S. Geological Survey Scientific Investigations Report, p. 176.

Blom, A., Viparelli, E., & Chavarrías, V. (2016). The graded alluvial river: Profile concavity and downstream fining. *Geophysical Research Letters*, *43*(12), 6285–6293. https://doi.org/10.1002/grl.v43.12

Brownlie, W. R. (1981). *Prediction of flow depth and sediment discharge in open channels* (Report No. KH-R-43A). W. M. Keck Laboratory of Hydraulics and Water Resources, California Institute of Technology, Pasadena, California.

Calazans, G. M., Pinto, C. C., da Costa, E. P., Perini, A. F., & Oliveira, S. C. (2018). The use of multivariate statistical methods for optimization of the surface water quality network monitoring in the Paraopeba River basin, brazil. *Environmental Monitoring and Assessment*, *190*(8), 1–17. https://doi.org/10.1007/s10661-018-6873-2

CPRM-ANA (2015). *Monitoramento Especial da bacia do Rio Doce. Relatorio 1: Acompanhamento da onda de cheia* (Technical report). Serviço Geológico do Brasil (SGB) e Agência Nacional de Águas (ANA). (in Portuguese).

CPRM, ANA, COPASA, and IGAM (2019). *Monitoramento Especial da Bacia Do Rio Paraopeba (Relatório 1: Monitoramento Hidrológico e Sedimentométrico)* (Technical report). Belo Horizonte. (in Portuguese).

Cui, Y., & Parker, G. (1999). *Sediment transport and deposition in the Ok Tedi-Fly River system, Papua New Guinea: The modeling of 1998–1999* (Technical report). St. Anthony Falls Laboratory, University of Minnesota, Minneapolis.

de Carvalho, R. P., Magalhães Jr, A. P., & de Paula Barros, L. F. (2021). Hydrogeomorphological impacts of the Córrego do Feijão iron tailings dam break – Minas Gerais state, Brazil. *Caderno de Geografia*, *31*(65), 518–545. https://doi.org/10.5752/P.2318-2962.2021v31n65p518

do Carmo, F. F., Kamino, L. H. Y., Junior, R. T., de Campos, I. C., Silvino, G., de Castro, K. J. d. S. X., Mauro, M. L., Rodrigues, N. U. A., Miranda, M. P. d. S., & Pinto, C. E. F. (2017). Fundão tailings dam failures: The environment tragedy of the largest technological disaster of Brazilian mining in global context. *Perspectives in Ecology and Conservation*, *15*(3), 145–151. https://doi.org/10.1016/j.pecon.2017.06.002

Duan, Q., Sorooshian, S., & Gupta, V. (1992). Effective and efficient global optimization for conceptual rainfall-runoff models. *Water Resources Research*, *28*(4), 1015–1031. https://doi.org/10.1029/91WR02985

Engelund, F., & Hansen, E. (1967). A monograph on sediment transport in alluvial streams. *Technical University of Denmark 0stervoldgade 10, Copenhagen K.*

Freer, J., Beven, K., & Ambroise, B. (1996). Bayesian estimation of uncertainty in runoff prediction and the value of data: An application of the GLUE approach. *Water Resources Research*, *32*(7), 2161–2173. https://doi.org/10.1029/95WR03723

Garcia, M. H. (2008). Sediment transport and morphodynamics (chapter 2). In M. H. Garcia (Ed.), *Sedimentation engineering: Processes, measurements, modeling, and practice* (pp. 21–163). ASCE Press.

Ghahramani, N., Chen, H. J., Clohan, D., Liu, S., Llano-Serna, M., Rana, N. M., McDougall, S., Evans, S. G., & Take, W. A. (2022). A benchmarking study of four numerical runout models for the simulation of tailings flows. *Science of the Total Environment*, *827*, 1–18. https://doi.org/10.1016/j.scitotenv.2022.154245

Gibson, S., Moura, L. Z., Ackerman, C., Ortman, N., Amorim, R., Floyd, I., Eom, M., Creech, C., & Sánchez, A. (2022). Prototype scale evaluation of non-newtonian algorithms in HEC-RAS: Mud and debris flow case studies of Santa Barbara and Brumadinho. *Geosciences (Switzerland)*, *12*(3), 1–23.

Granger, B., Laval, B., Vagle, S., Petticrew, E. L., Owens, P. N., & Baldwin, S. A. (2022). Initial distribution and interannual decrease of suspended sediment in a two-basin lake following a massive mine tailings spill: Quesnel Lake, BC, Canada. *Water Resources Research*, *58*(5), 1–17. https://doi.org/10.1029/2021WR030574

Gupta, H. V., Kling, H., Yilmaz, K. K., & Martinez, G. F. (2009). Decomposition of the mean squared error and NSE performance criteria : Implications for improving hydrological modelling. *Journal of Hydrology*, *377*(1-2), 80–91. https://doi.org/10.1016/j.jhydrol.2009.08.003

Guy, H., Simons, D. B., & Richardson, E. (1966). *Summary of alluvial channel data from flume experiments, 1956-61*. U.S. Geology Survey (pp. 1–104).

Hirano, M. (1971). River-bed degradation with armoring. In Engineers, J. S. o. C. (Ed.), *Proceedings of the Japan Society of Civil Engineers (Vol. 1971, No. 195, in Japanese)* (pp. 55–65). Collection of Papers and Reports of the Civil Engineering Society.

Hoey, T. B., & Ferguson, R. (1994). Numerical simulation of downstream fining by selective transport in gravel bed rivers: Model development and illustration. *Water Resources Research*, *30*(7), 2251–2260. https://doi.org/10.1029/94WR00556

Hudson-Edwards, K. (2016). Tackling mine wastes. *Science (New York, N.Y.)*, *352*(6283), 288–290. https://doi.org/10.1126/science.aaf3354

IBGE (2010). IBGE censo 2010: Brazilian population census. *Instituto Brasileiro de Geografia e Estatística*. Retrieved June 1, 2022.

IGAM (2010). *Monitoramento da qualidadde das águas superficiais na sub-bacia do rio Paraopeba em 2009* (Technical report). CETEC. IGAM – Instituto Mineiro de Gestão das Águas. Governo de Minas. (in Portuguese).

IGAM (2013). *Identificação de municípios com condição crítica para a qualidade de água na bacia do rio Paraopeba* (Technical report), IGAM – Instituto Mineiro de Gestão das Águas e Secretaria de Meio Ambiente e Desenvolvimento Sustentável, Belo Horizonte. (in Portuguese).

Julien, P. Y., & Klaassen, G. J. (1995). Sand-dune geometry of large rivers during floods. *Journal of Hydraulic Engineering*, *121*(September), 657–663. https://doi.org/10.1061/(ASCE)0733-9429(1995)121:9(657)

Karim, M. F. (1981). *Computer-based predictors for sediment discharge and friction factor of alluvial streams* [Ph.d. thesis]. The University of Iowa.

Karim, M. F., & Kennedy, J. F. (1982). *Ialluvial: A computer-based flow- and sediment-routing model for alluvial streams and its application to the Missouri river* (Technical Report 250). Iowa Institute of Hydraulic Research. The University of Iowa, Iowa City.

Kraft, D. (1988). A software package for sequential quadratic programming. *Forschungsbericht- Deutsche Forschungs- und Versuchsanstalt fur Luft- und Raumfahrt*.

Laureano, F. V., Kwitko-Ribeiro, R., Guimarães, L., & Leão, L. P. (2022). Mineralogical fingerprint of iron ore tailings in paraopeba river bedload sediments after the B1 dam failure in Brumadinho, MG (Brazil). *Minerals*, *12*(6), 716. https://doi.org/10.3390/min12060716

Lindenschmidt, K.-E., Sabokruhie, P., & Rosner, T. (2022). Modelling transverse mixing of sediment and vanadium in a river impacted by oil sands mining operations. *Journal of Hydrology: Regional Studies*, *40*, Article 101043.

Lumbroso, D., Davison, M., Body, R., & Petkovšek, G. (2021). Modelling the Brumadinho tailings dam failure, the subsequent loss of life and how it could have been reduced. *Natural Hazards and Earth System Sciences*, *21*(1), 21–37. https://doi.org/10.5194/nhess-21-21-2021

Marron, D. C. (1989). The transport of mine tailings as suspended sediment in the Belle Fourche River, west-central South Dakota, USA. In *Sediment and environment* (number 184, pp. 19–26). IAHS.

Martínez-Aranda, S., García, R., & García-Navarro, P. (2022). GPU-accelerated developments for the realistic simulation of large-scale mud/debris flows. In *Proceedings of the 39th IAHR World Congress* (number June, pp. 4240–4249). International Association for Hydro-Environment Engineering and Research (IAHR).

Molinas, A., & Wu, B. (2010). Transport of sediment in large sand-bed rivers. *Journal of Hydraulic Research*, *39*(2001–2), 135–146.

Muttil, N., & Jayawardena, A. (2008). Shuffled complex evolution model calibrating algorithm: Enhancing its robustness and efficiency. *Hydrological Processes: An International Journal*, *22*(23), 4628–4638. https://doi.org/10.1002/hyp.v22:23

Naito, K., Ma, H., Nittrouer, J. A., Zhang, Y., Wu, B., Wang, Y., Fu, X., & Parker, G. (2019). Extended Engelund–Hansen type sediment transport relation for mixtures based on the sand-silt-bed Lower Yellow River, China. *Journal of Hydraulic Research*, *57*(6), 770–785. https://doi.org/10.1080/00221686.2018.1555554

Nino, Y., Lopez, F., & Garcia, M. (2003). Threshold for particle entrainment into suspension. *Sedimentology*, *50*(2), 247–263. https://doi.org/10.1046/j.1365-3091.2003.00551.x

Palu, M. C., & Julien, P. Y. (2019). Modeling the sediment load of the Doce River after the Fundão tailings dam Collapse, Brazil. *Journal of Hydraulic Engineering*, *145*(5), 05019002-1–05019002-14. https://doi.org/10.1061/(ASCE)HY.1943-7900.0001582

Paola, C., Parker, G., Seal, R., Sinha, S. K., Southard, J. B., & Wilcock, P. R. (1992). Downstream fining by selective deposition in a laboratory flume. *Science (New York, N.Y.)*, *258*(December), 1757–1760. https://doi.org/10.1126/science.258.5089.1757

Parker, G. (1991). Selective sorting and abrasion of river gravel. I: Theory. *Journal of Hydraulic Engineering*, *117*(2), 131–147. https://doi.org/10.1061/(ASCE)0733-9429(1991)117:2(131)

Parker, G. (2004). 1D sediment transport morphodynamics e-book with applications to rivers and turbidity currents.

Pedocchi, F., & García, M. H. (2006). Evaluation of the LISST-ST instrument for suspended particle size distribution and settling velocity measurements. *Continental Shelf Research*, *26*(8), 943–958. https://doi.org/10.1016/j.csr.2006.03.006

Rahuel, J., Holly, F., Chollet, J., Belleudy, P., & Yang, G. (1989). Modeling of riverbed evolution for bedload sediment mixtures. *Journal of Hydraulic Engineering*, *115*(11), 1521–1542. https://doi.org/10.1061/(ASCE)0733-9429(1989)115:11(1521)

Robertson, P. K., De Melo, L., Williams, D. J., & Wilson, G. W. (2019). *Report of the Expert Panel on the Technical Causes of the Failure of Feijão Dam I* (Technical report).

Rojas-Aguirre, A. F., & Garcia, M. H. (2025). Experiments on entrainment of tailings into suspension in an annular flume. *Journal of Hydraulic Engineering*, *151*(1), Article 04024065. https://doi.org/10.1061/JHEND8.HYENG-14095

Salgado Terêncio, D. P., Leal Pacheco, F. A., Farias do Valle Junior, R., M. M. Abreu Pires de Melo Silva, Tarlé Pissarra, T. C., M. Carvalho de Melo, Valera, C. A., & Sanches Fernandes, L. F. (2023). The Igarapé weir decelerated transport of contaminated sediment in the Paraopeba River after the failure of the B1 tailings dam (Brumadinho). *International Journal of Sediment Research*, *38*, 673–697.

Soares Sobrinho, V. d. P., & Graça, N. G. (2009). Retiro Baixo hydropower plant on the Paraopeba River. In *Main Brazilian dams III. Design, construction and performance* (pp. 341–355). Brazilian Committee on Dams and International Commission on Large Dams.

Vale and Arcadis (2020). *Caracteriçao Geológica dos testemunhos Coletados no Rio Paraopeba – MG* (Technical report). Brumadinho, Brazil. (in Portuguese).

Vale and Potamos (2020). *Modelo Computacional de Transporte de Sedimentos* (Technical Report RL-3000GG-X-00008). Brumadinho, Brazil. (in Portuguese).

Vale and Saga (2021). *Modelamento Geológico na calha do Rio Paraopeba* (Technical report). Brumadinho, Brazil. (in Portuguese).

Viparelli, E., Sequeiros, O. E., Cantelli, A., Wilcock, P. R., & Parker, G. (2010). River morphodynamics with creation/consumption of grain size stratigraphy 2: Numerical model. *Journal of Hydraulic Research*, *48*(6), 727–741. https://doi.org/10.1080/00221686.2010.526759

Viparelli, E., Solari, L., & Hill, K. M. (2015). Downstream lightening and upward heavying: Experiments with sediments differing in density. *Sedimentology*, *62*(5), 1384–1407. https://doi.org/10.1111/sed.2015.62.issue-5

Vrugt, J. A., Gupta, H. V., Bouten, W., & Sorooshian, S. (2003). A shuffled complex evolution metropolis algorithm for optimization and uncertainty assessment of hydrologic model parameters. *Water Resources Research*, *39*(8), 1–14.

Wang, K., Yang, P., Yu, G., Yang, C., & Zhu, L. (2020). 3D numerical modelling of tailings dam breach run out flow over complex terrain: A multidisciplinary procedure. *Water (Switzerland)*, *12*(9), 1–14.

Wright, S., & Parker, G. (2005). Modeling downstream fining in sand-bed rivers. I: Formulation. *Journal of Hydraulic Research*, *43*(6), 613–620. https://doi.org/10.1080/00221680509500381

Yang, C. T. (1973). Incipient motion and sediment transport. *Journal of the Hydraulics Division*, *99*(10), 1679–1704. https://doi.org/10.1061/JYCEAJ.0003766

Yang, X. S., & Deb, S. (2009). Cuckoo search via Lévy flights. In *2009 World Congress on Nature and Biologically Inspired Computing, NABIC 2009 – Proceedings* (pp. 210–214). IEEE.

Appendices

Appendix 1. Derivation of equation that describes the evolution of density in the active layer

For the control volume defined in Figure 3 (Section 2.3), the 1D sediment conservation equation in terms of mass transport rate per unit width, is defined as:

$$\frac{\partial}{\partial t}\int_0^{\eta} \rho_i' f_i' (1-\lambda_p)\Delta x\, dz = \left[\rho_{i-in} q_{Ti}|_x - \rho_{i-out} q_{Ti}|_{x+\Delta x}\right] \quad (A1)$$

$$(1-\lambda_p)\frac{\partial}{\partial t}\int_0^{\eta} \rho_i f_i'\, dz = -\frac{\partial}{\partial x} g_{Ti} \quad (A2)$$

The control volume is divided into two regions: active layer and substrate layer, for which the volume (f_i') and density fractions (ρ_i') in the ith grain size are defined as:

$$f'_i(x,z,t) = \begin{cases} F_i(x,z,t), & \eta - L_a < z < \eta \\ f_{Ti}(x,z), & \eta_b < z \le \eta - L_a \end{cases} \quad (A3)$$

$$\rho'_i(x,z,t) = \begin{cases} \rho_i(x,z,t), & \eta - L_a < z < \eta \\ \rho_{si}(x,z), & \eta_b < z \le \eta - L_a \end{cases} \quad (A4)$$

Based on the previous definitions, the integral in Equation (A2) can be defined and evaluated as:

$$\frac{\partial}{\partial t}\int_{\eta_b}^{\eta} \rho_i' f_i'\, dz = \frac{\partial}{\partial t}\left(\int_{\eta_b}^{\eta-La} \rho_i' f_i'\, dz + \int_{\eta-La}^{\eta} \rho_i' f_i'\, dz\right)$$

$$\frac{\partial}{\partial t}\int_{\eta_b}^{\eta} \rho_i' f_i'\, dz = \frac{\partial}{\partial t}\left(\rho_i' f_i' z\Big|_{\eta_b}^{\eta-La} + \rho_i' f_i' z\Big|_{\eta-La}^{\eta}\right)$$

$$\frac{\partial}{\partial t}\int_{\eta_b}^{\eta} \rho_i' f_i'\, dz = \frac{\partial}{\partial t}\left(\rho_{Ii} f_{Ii}(\eta - La) + \rho_i F_i La\right) \quad (A5)$$

The previous equation can be rewritten as:

$$\frac{\partial}{\partial t}\int_0^{\eta} \rho_i' f_i'\, dz = (F_i\rho_i - \rho_{Ii} f_{Ii})\frac{\partial L_a}{\partial t} + \rho_{Ii} f_{Ii}\frac{\partial \eta}{\partial t} + La\frac{\partial F_i \rho_i}{\partial t} \quad (A6)$$

Substituting Equation (A6) into Equation (A2) we get:

$$(1-\lambda_p)\left[(F_i\rho_i - \rho_{Ii} f_{Ii})\frac{\partial L_a}{\partial t} + \rho_{Ii} f_{Ii}\frac{\partial \eta}{\partial t} + La\frac{\partial F_i \rho_i}{\partial t}\right] = -\frac{\partial g_{Ti}}{\partial x}. \quad (A7)$$

The total mass transport rate g_T, the bulk density ρ_a and the bulk density for the interfacial exchange ρ_I can be calculated as the summation of all the fractions:

$$g_T = \sum_{n=1}^{N} g_{Ti}, \quad \rho_I = \sum_{n=1}^{N} f_{Ii}\rho_{Ii}, \quad \rho_a = \sum_{n=1}^{N} F_i \rho_i \quad (A8)$$

Based on the previous relations and with some algebra manipulation, Equation (A7) turns into the form:

$$\frac{\partial \eta}{\partial t} = -\frac{1}{\rho_I(1-\lambda_p)}\frac{\partial g_T}{\partial x} - \left(\frac{\rho_a}{\rho_I} - 1\right)\frac{\partial L_a}{\partial t} - \frac{La}{\rho_I}\frac{\partial \rho_a}{\partial t} \quad (A9)$$

Appendix 2. Simplified equations for the Paraopeba river

In our analysis, we consider only two sediment fractions: iron tailings and ambient sand. We define F_s as the fraction of ambient sand and F_T as the fraction of iron tailings, with their relationship given by:

$$F_s = 1 - F_T \quad (A10)$$

Considering only these two sediment fractions, and only two representative densities for each fraction, the density within the active layer is calculated based on Equation (A8) as follows:

$$\rho_a = \rho_s F_s + \rho_T F_T \quad (A11)$$

where ρ_s and ρ_T are the densities of the ambient sand and iron tailings, respectively. Based on Equations (A10) and (A11), the rate of change of the density in the active layer ($\partial\rho_a/\partial t$) can be written as:

$$\frac{\partial \rho_a}{\partial t} = \frac{\partial F_s}{\partial t}(\rho_s - \rho_T) \quad (A12)$$

As $\partial\eta/\partial t$ is also a function of the rate of change of the thickness of the active layer, we use the equation proposed by Julien and Klaassen (1995) to determine this rate (Equation (A13)):

$$L_a = \alpha_D \Delta_{dune} = \alpha_D \Delta_{dune} = \alpha_D \xi H \left(\frac{D_{sg}}{H}\right)^{0.3} \quad (A13)$$

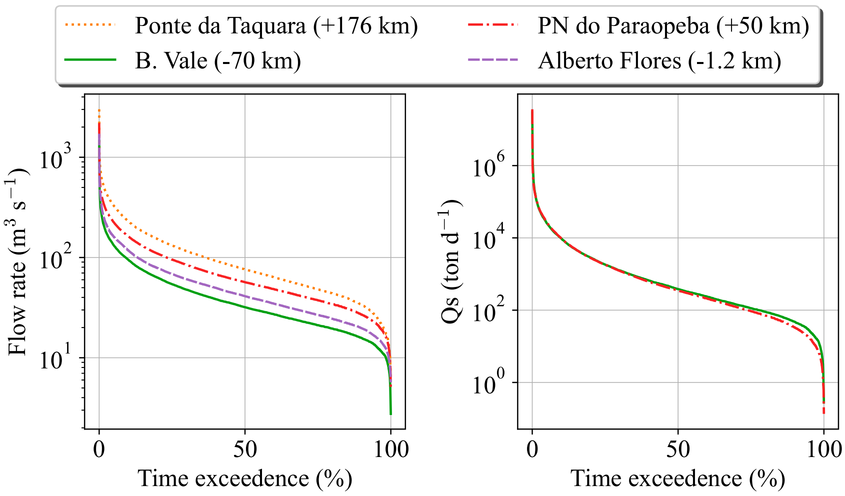

Figure A1. Flow duration curves (FDC) and suspended sediment duration curves (SSDC) for streamgages at Ponte da Taquara, Belo Vale, Ponto Novo do Paraopeba, and Alberto Flores. Positive and negative signs denote distances upstream and downstream of the Ferro Carvão Creek confluence, respectively.

Consequently, the rate of change of L_a is estimated as follows:

$$\frac{\partial L_a}{\partial t} = \alpha_D \xi \left[0.7 \frac{D_{sg}}{H^{0.3}} \frac{\partial H}{\partial t} + 0.3 \frac{H^{0.7}}{D_{sg}^{0.7}} \frac{\partial D_{sg}}{\partial t} \right] \tag{A14}$$

As we are considering a steady-state flow condition, the previous equation can be simplified as:

$$\frac{\partial L_a}{\partial t} = 0.3 \alpha_D \xi \frac{H^{0.7}}{D_{sg}^{0.7}} \frac{\partial D_{sg}}{\partial t} \tag{A15}$$

To determine $\partial D_{sg}/\partial t$, we use the definition of D_{sg}:

$$D_{sg} = 2^{\bar{\psi}}, \quad \bar{\psi} = \sum_{n=1}^{N} \psi_i F_i \tag{A16}$$

Based on the previous definition, and taking into consideration the two fractions considered in this study, it is possible to determine the rate of change of D_{sg} as:

$$\frac{\partial D_{sg}}{\partial t} = D_{sg} \ln(2)(\psi_s - \psi_T) \frac{\partial F_s}{\partial t} \tag{A17}$$

where $\psi_s = \log_2 D_s$, and $\psi_T = \log_2 D_T$. Substituting Equation (A17) into Equation (A15) and with some algebra manipulation, Equation (A15) turns into:

$$\frac{\partial L_a}{\partial t} = 0.3 L_a \ln(2)(\psi_s - \psi_T) \frac{\partial F_s}{\partial t} \tag{A18}$$

Substituting Equations (A18) and (A12) into Equation (A9) yields:

$$\frac{\partial \eta}{\partial t} = -\frac{1}{\rho_I (1 - \lambda_p)} \frac{\partial g_T}{\partial x} - \Bigg[0.3 L_a \ln(2)(\psi_s - \psi_T) \times \left(\frac{\rho_a}{\rho_I} - 1 \right) + \frac{L_a}{\rho_I} (\rho_s - \rho_T) \Bigg] \frac{\partial F_s}{\partial t} \tag{A19}$$

Assuming $\rho_T = \rho_{IT}$, $\rho_s = \rho_{Is}$, and substituting Equations (A18), (A19) into (A7), we obtain:

$$(1 - \lambda_p) \Bigg[(F_s \rho_s - \rho_s f_{I1}) \left(0.3 L_a \ln(2)(\psi_s - \psi_T) \frac{\partial F_s}{\partial t} \right) + \rho_s f_{Is} \Bigg(-\frac{1}{\rho_I (1 - \lambda_p)} \frac{\partial g_T}{\partial x} - 0.3 L_a \ln(2) \times (\psi_s - \psi_T) \left(\frac{\rho_a}{\rho_I} - 1 \right) \frac{\partial F_s}{\partial t} - \frac{L_a}{\rho_I} (\rho_s - \rho_T) \frac{\partial F_s}{\partial t} \Bigg) + L_a \rho_s \frac{\partial F_s}{\partial t} \Bigg] = -\frac{\partial g_{Ts}}{\partial x} \tag{A20}$$

After some mathematical manipulation it is possible to solve for $\partial F_s/\partial t$:

$$\rho_s \frac{\partial F_s}{\partial t} = \frac{1}{(1 - \lambda_p) L_a} \left[-\frac{\partial g_{Ts}}{\partial x} + \frac{\rho_s f_{Is}}{\rho_I} \frac{\partial g_T}{\partial x} \right] \times \left[\frac{1}{(1 + K_1) + (1 + K_2) - 1} \right] \tag{A21}$$

where:

$$K_1 = 0.3 \ln(2)(\psi_s - \psi_T) \left(F_s - f_{Is} \frac{\rho_a}{\rho_I} \right),$$

$$K_2 = -f_{Is} \frac{(\rho_s - \rho_T)}{\rho_I}$$

Appendix 3. Mean annual sediment discharge and dominant discharge

This appendix outlines the methodology in this work to estimate the mean annual sediment discharge and dominant discharge. The inputs to estimate these morphological flows are as follows:

- Flow duration curve (FDC): This curve is constructed from extensive flow time series, including morphologically representative discharge events with high return periods. It is recommended to have a fine time resolution (i.e preferably hourly). The FDCs and the sediment load duration curves for the streamgages reported are shown in Figure A1.
- The relationship between flow discharge and sediment flow discharge can be established either through a rating curve based on observed data or a sediment transport equation (e.g. Engelund–Hansen, Brownlie, Cruickshank–Maza). In this case we used the rating curves developed by Vale at streamgages Ponte Novo do Paraopeba. For Porto Mesquita and at Melo Franco (P0, see Figure 1), we developed a discharge-sediment load rating curve based on the dataset developed by Vale and the historical data reported by CEMIG.
- Cut-off size for wash load: In this analysis, we excluded the wash load fractions since they do not play a role in the

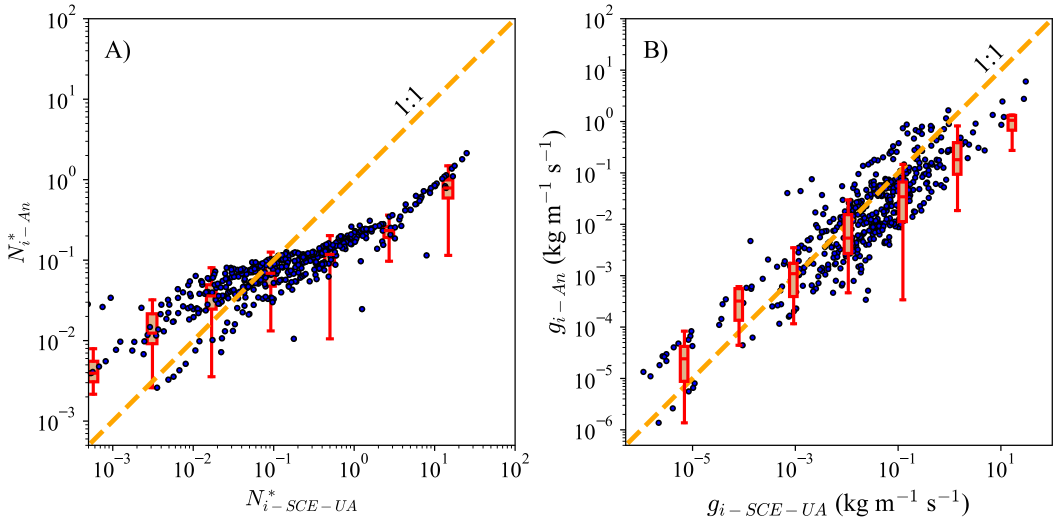

Figure A2. Comparison between simulation results using the calibration parameters determined by An et al. (2020) and by the SCE method (Table A3). (a) Dimensionless sediment transport rate N_i. (b) Dimensionless sediment transport rate per unit width for the diameter in the ith range size, q_i. Boxplots are displayed within arbitrary regular-spacing bins.

Table A1. Steps to calculate mean total sediment discharge.

Columns I – II Flow range Q_i [l^3s^{-1}]		Column III Flow average $\overline{Q_i}$ [l^3s^{-1}]	Column IV Frequency f_i %	Column V Sediment discharge Qs_i [l^3s^{-1}]	Column VI $Qs_i * f_i$ [l^3s^{-1}]
Lower limit	Higher limit				
Q_{N-1}	Q_N	$\overline{Q_n}$	f_n	Qs_n	$Qs_n * f_n$
Q_{N-2}	Q_{N-1}	$\overline{Q_{n-1}}$	f_{n-1}	Qs_{n-1}	$Qs_{n-1} * f_{n-1}$
⋮		⋮	⋮	⋮	⋮
Q_1	Q_2	$\overline{Q_1}$	f_1	Qs_1	$Qs_1 * f_1$
					$Qs = \sum_{i=1}^{N} Qs_i * f_i$

morphological changes. Commonly for sand-bed rivers, the cut-off size is 62.5 μm.

Based on the previous inputs, we have estimated the dominant discharge using the information provided in Table A1.

- Column I and II: the flow records are discretized in different classes. Column I and Column II are the lower and upper limits at each class.
- Column III: corresponds to the mean flow at each class.
- Column IV: this is the frequency of flow rates associated with each class. It is estimated as the difference between the frequencies for the upper and lower limits.
- Column V: these values come from a rating curve developed from measurements or a sediment transport relation.
- Column VI: the product between Columns IV and V and represents the sediment flow contribution at each class.

The sum of Column VI represents the mean annual sediment discharge (Qs). The dominant discharge is the flow average value (in Column III) that is associated with the mean annual sediment discharge, Qs.

Due to the limited historical records in the river before the accident, this mean annual sediment load was calculated at three different locations that are shown in Table A2.

Appendix 4. Sediment transport equation

A.1. Comparative analysis of calibrated equation in relation to An et al. (2020) equation

Herein we compare the outcome of the SEH by using the calibrated parameters determined by An et al. (2020) and those calibrated in this study (Table A3). To perform this comparison, we used the dataset from the Paraopeba River. The comparison of the dimensionless parameters depicted in Figure A2a shows that the N_i^* values estimated by the parameters proposed by An et al. (2020) tend to be larger than those proposed in this study when $N_i^* \sim 0.05$, and lower otherwise. However, the q_i scatter plot reveals a propensity for lower values when we consider the equation proposed by An et al. (2020) (Figure A2b).

The previous calibrated parameters and objective function values are comparable across different optimization methods, including sequential least squares programming (Kraft, 1988), cuckoo search algorithm (X. S. Yang & Deb, 2009), and the ‘ brute force’ method with uniform distribution (Table A4).

The sediment transport rate differences between the study conducted by An et al. (2020) and this study may be attributed to variations in laboratory conditions (Guy et al., 1966) used to calibrate the SEH equation proposed by An et al. (2020) and the actual conditions in the Paraopeba River. These differences can be ascribed to various anthropogenic pressures:

- **Sand mining:** This is a common activity along the river and across its basin to meet the construction demands in the metropolitan area of Belo Horizonte (IGAM, 2010).
- **Dammed tributaries:** Three reservoirs were built to supply water for the Belo Horizonte metropolitan area (Manso River, Serra Azul, and Vargem das Flores).
- **Inline structures:** Upstream of the Retiro Baixo Reservoir, two spillways create a headpond for electricity generation (Salto do Paraopeba Run of the River and Igarapé). The coarse material tends to be retained upstream of these structures (de Carvalho et al., 2021).

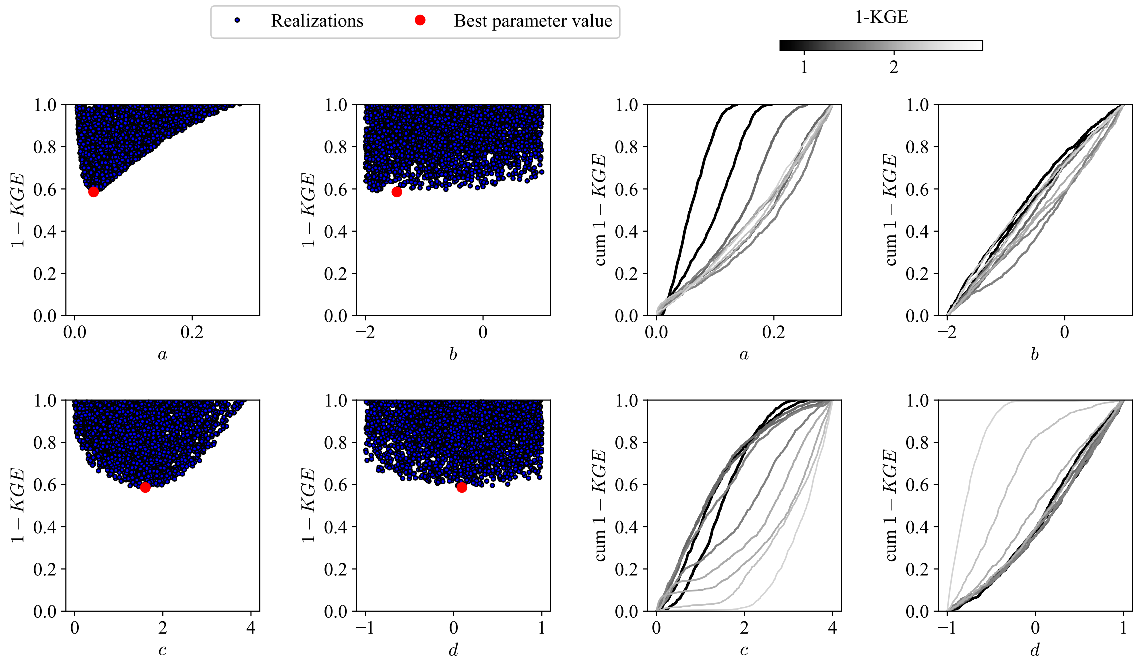

Figure A3. Identifiability and parametric sensitivity analysis for the Engelund Hansen model for mixtures. Left: Identifiability analysis for each parameter via dotty plots (the best set of parameters is represented in red dots). Right: regional sensitivity analysis for each parameter in cumulative frequency distribution form.

Table A2. Mean annual sediment load and dominant discharge along the Paraopeba River.

Location	Mean annual sediment load (Mton day^{-1})	Dominant Discharge (m^3 s^{-1})	Flow time series source	Sediment sources
Melo Franco (−10 km)	0.21	116.9	Alberto Flores (1963–2020)	Rating curve at Melo Franco P0
Ponte Novo do Paraopeba (+50 km)	0.24	165.9	Ponte Novo do Paraopeba (1938–2018)	Ponte Novo do Paraopeba (1938–2018)
Porto Mesquita	0.25	205.5	Porto Mesquita (1977–2019)	Porto Mesquita (1977–2019)

Table A3. Calibrated parameters from the recalibrated SEH equation and from An et al. (2020).

	SCE-UA	An et al. (2020)
a	0.0323	0.037
b	−1.466	0.445
c	1.6031	0.876
d	0.0941	−0.348
1-*KGE*	0.589	0.833

- **Sand–tailings mixtures:** The insertion of the iron tailings in this riverine system changes the GSD and density of the bed material as it mixes with the natural sediment.
- **Bedrock outcrops:** Although this item does not correspond to anthropogenic pressure, the river is controlled laterally and vertically by bedrock outcrops that differ from the laboratory conditions described by Guy et al. (1966).

A.2. Sensitivity analysis

Identifiability and sensitivity analyses were performed with the SEH equation calibrated in this study. These analyses are conducted via dotty plots and regional sensitivity analysis (RSA, Freer et al., 1996) by using a uniform distribution sampling parameter space (Figure A3). Ten thousand realizations are evaluated, and each set of parameters is plotted against the objective function, 1−KGE (dotty plots). The red dots represent the best set of parameters obtained by the SCE-UA algorithm. Uniform scatter points denote low sensitivity to the objective function, while high sensitivity is represented by a clear minimum on the dotty plot. Likewise, the RSA indicates low sensitivity when the ten cumulative functions are parallel and close to each other. This qualitative analysis showed that the sensitive and identifiable parameters are *a*, *c* and *d*. The latter two were expected to be sensitive as they associated with the power parameter (B_i) in Equation (11). *b* is the less sensitive parameter, and it can take the same value found by An et al. (2020).

Appendix 5. 1D Hydraulic analysis assuming fix bed

The morphology of the Paraopeba River is characterized by a pool-riffle sequence in which the bedrock outcrops control the vertical and lateral erosion in the river. A steady state 1-D hydraulic analysis, assuming fix bed (using the real cross-sections from bathymetry performed in February 2019) show that high flows tend to maintain a more uniform slope and diminish the effect of these morphological sequences in which the flow tends to be critical or near-critical (Figure A4).

Table A4. Calibrated parameters using different optimization methods.

Method/parameters	*a*	*b*	*c*	*d*	1-*KGE*
SCE-UA	0.0323	−1.466	1.6031	0.0941	0.58582
Cuckoo search algorithm	0.0329	−1.327	1.6105	0.0659	0.58611
Sequential least squares programming	0.0323	−1.383	1.6165	0.0739	0.58589
'Brute force' uniform distribution	0.0353	−1.630	1.7505	0.2352	0.5922

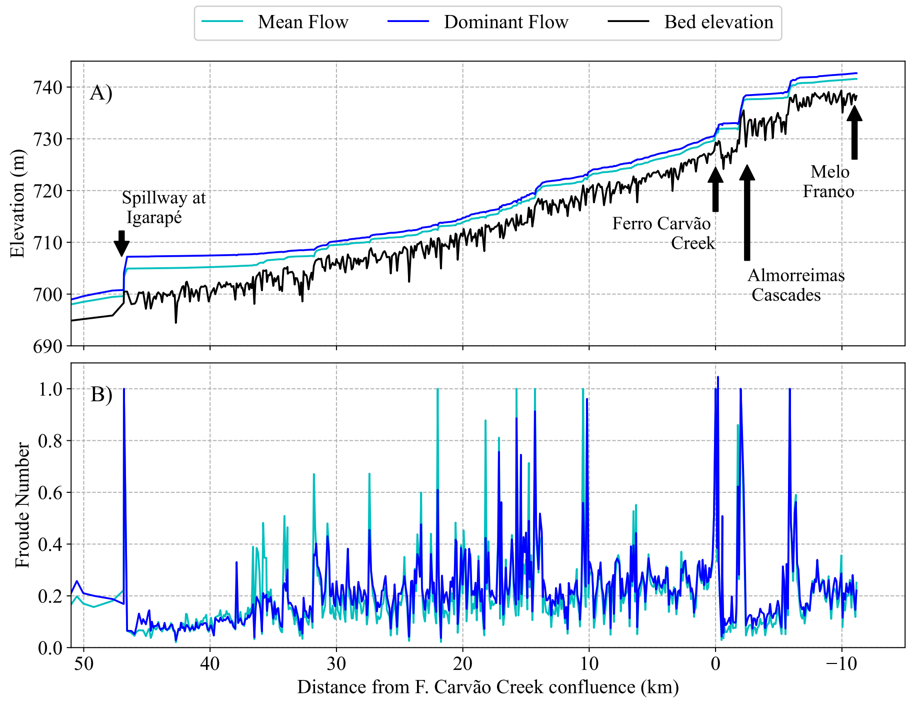

Figure A4. Hydraulic vertical profile and Froude number from Melo Franco to the spillway at Igarapé for a steady-state flow condition assuming flow dominant discharge (116.9 $m^3 s^{-1}$) and mean annual flow discharge (61.4 $m^3 s^{-1}$, based on the flow discharge records at Alberto Flores streamgage). This analysis is conducted for a fixed-bed condition using a bathymetry conducted in February 2019.

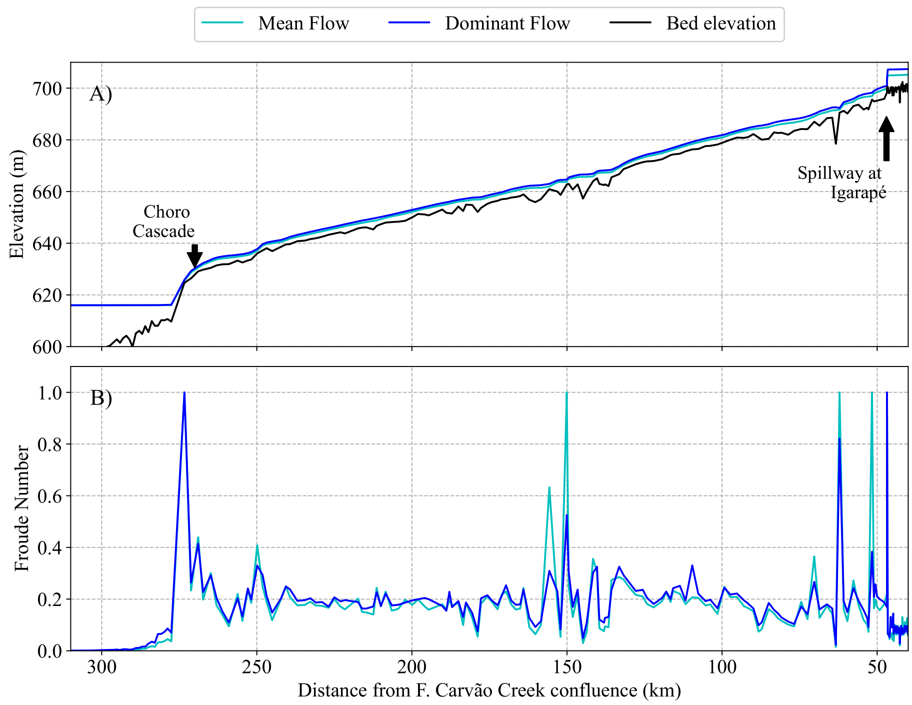

Figure A5. Hydraulic vertical profile and Froude number from the spillway at Igarapé to the Headwaters of Retiro Baixo Reservoir for a steady-state flow condition assuming flow dominant discharge (116.9 $m^3 s^{-1}$) and mean annual flow discharge (61.4 $m^3 s^{-1}$, based on the flow discharge records at Alberto Flores streamgage). This analysis is conducted for a fixed-bed condition using a bathymetry conducted in February 2019.